Structural Study of Doped CdSe Nanoeires Using X-ray Scattering Method

Masterarbeit

Zur Erlangung des akademischen Grades

Master of Science

(M.Sc.)

der Universität Siegen

Department Physik

vorgelegt von

Krishna Prasad Kandel

April 2012

Table of Contents

Chapter 1

1. Introduction

The low dimensional crystalline semiconductor nanostructures having size several nanometers to micrometer have attraction due to their unique optical, electrical, mechanical, and chemical properties which cannot be found in thin film and bulk materials. The research on nanomaterials has focused on the colloidal semiconductor nanocrystal because of their size tunable electronic characteristic; originate from the quantum confinement effect of charge carriers (electrons and holes) in one dimension. Cadmium selenide (CdSe) is an II-IV semiconductor material; it has a direct energy band-gap (1.74eV at room temperature) and is an excellent candidate for device performance. The colloidal CdSe nanostructures play an important role in technical applications such as light-emitting diodes, lasers, and biological labels[1, 2].

Doping-the intentional incorporation of impurities into a semiconductor nanowires alters the properties of a semiconductors in controllable and desirable ways. Specifically, the paramagnetic-ion-doped semiconductor nanostructures, such as dots, rods, wires, films became more attraction due to their fascinating properties and potential applications in solar cells[3], bioimaging[2, 4], spintronic[5] and quantum interference information processing. The doping of the nanomaterial can change the structural parameters and electronic properties. For example; in solar cells doping may protect the material against photo-oxidation[6], for magnetic material the doping enhance the quantum mechanical spins in nanocrystal[7]. Therefore, structural study of nanomaterials is a crucial issue for the development of nanoscale device.

In our study, the undoped and doped (Mn, Co, Fe) CdSe nanowires were nucleated and grown via solution-liquid-solid (SLS) method using bismuth (Bi) nanocatalysts. These chemical synthesized nanowires crystallize in either hexagonal wurtzite (W) phase or cubic zinc-blende (ZB) phase, while admixture of both phases are also possible[8]. The shape and size of the randomly oriented nanowires can be controlled by reaction conditions like as molecular

precursors, concentration and concentration ratios, organic ligands, reaction time and temperature[9]. Because of the anisotropic growth, both doped and undoped NWs are elongated in the 001-direction of the wurtzite lattice forming nanowires. Historically, the controlled doping of CdSe NWs with Mn was failed[10, 11] till 2008. In 2010, Zhen Li and his group have grown Mn doped CdSe NWs[12] using SLS approach for the first time.

It was demonstrated that Mn-doped CdSe NWs generated by a wet chemical (SLS) method, give potentially cheaper and magnetically active quantum wires. Because of the small diameters (8-19)nm of the Nws single crystal diffraction techniques cannot be used, therefore structural characterizations of these NWs are examined by X-ray powder diffraction technique. The X-ray powder diffraction pattern of NWs shows the admixture of wurtzite and ZB phases. Peak broadening effects are seen on the doped CdSe NWs caused by the size, doping influence, strain and mainly due to the stacking faults. Effects of Mn doping on the ratio of wurtzite to ZB structure units are examined to be decreasing within the doped NWs which is calculated by the ratio of intensities of certain reflections. The lattice constant c and strain along the NWs found to be increasing with increasing the doping concentration while the grain sizes of the NWs are decreasing with doping.

Two different approaches are used to analyze the simulated powder diffraction data, which is obtained by application of the Debye equation. The first one is the modeling of the scattering data in reciprocal space and another one is to model of the atomic pair distribution function (PDF) which can be obtained from the total scattering pattern[13]. The program [DISCUS] is used to create wurtzite/ZB mono-layers, stacking of these layers, to an appropriate length of the nanowire and calculate the powder patterns using Debye formula. The introduction of growth faults and deformation faults show a variation of peak broadening and intensities in diffraction pattern. For doping, the simulation of CdSe NWs is not yet well understood.

This work demonstrates the structural investigation of one dimensional magnetically active[5, 14, 15] doped CdSe NWs which are characterized by X-ray diffraction technique. Simulation creates the different models of CdSe NWs leading to calculate their diffraction patterns and compares qualitatively with the experimental diffraction pattern because many randomly oriented NWs from simulations.

Chapter 2

2. Characterization Method

Different methods can be used to characterize nanostructure materials such as transmission electron microscopy (TEM), scanning electron microscopy (SEM) and X-ray scattering methods. TEM and SEM are used for visualization and qualitative analysis of the size and shape of crystallites and structures of nano-materials while X-ray scattering is the method of choice for the quantitative analysis.

2.1 X-ray Scattering Method:-

X-ray scattering is an indispensable tool for structure determinations of crystalline material due to their unique diffraction pattern. X-rays are characterized by high energies and wavelengths that are commensurate with nanometer-sized structures.

2.2 Introduction of X-rays

X-rays are electromagnetic wave with typical wavelength ranging in between 10^{-8} m to 10^{-11}m. For diffraction purpose only short wavelength (few Angstrom to 0.1 Angstrom) are suited for probing structural arrangement of atoms and molecules in a wide range of material. They are produced by accelerating or decelerating the charged particles (electrons or positrons) in a stationary or rotating target. Thus, produced X-rays energy (E) is related to the wavelength (λ) as given by:

$$E = \frac{hc}{\lambda} \qquad (2.2.1)$$

where h is Planck's constant and c is the speed of light in vacuum. For experimental purpose we had to use two X-ray sources, one is home lab source where X-ray is produced from conventional X-ray tube and another is a Synchrotron source.

2.2.1 X-ray tubes

In an X-ray tube, an electron beam is accelerated across high voltage and bombards on the metal target where X-rays are produced. Electrons collide with the electron shell of atoms in the metal target decelerate resulting in an emitted continuous spectrum called Bremsstrahlung. In addition, the high energy electrons can eject electrons from the inner shells of the atoms of the target material. Then electrons from higher states drop down to fill the hole, emitting x-ray photons with precise energies associated with the difference between the atomic energy levels of the target atoms called characteristic radiation. The most intense line is the Kα doublet; it corresponds to the energy difference between the $2p_{x,\,y}$-1s ($K\alpha_1$) and the $2p_z$-1s ($K\alpha_2$) states. The energy level of $2p_x$ and $2p_y$ is equal but differ from that of the $2p_z$, therefore the intensity of $K\alpha_1$ line is double the intensity of $K\alpha_2$ line. The X-rays produced by transition of electrons from 3p-1s states called Kβ line which is less intense than the Kα line. An angular dispersive experiment mostly makes use of one of the Kα lines because its intensity is about 4 order higher than the intensity of Bremsstrahlung[16].

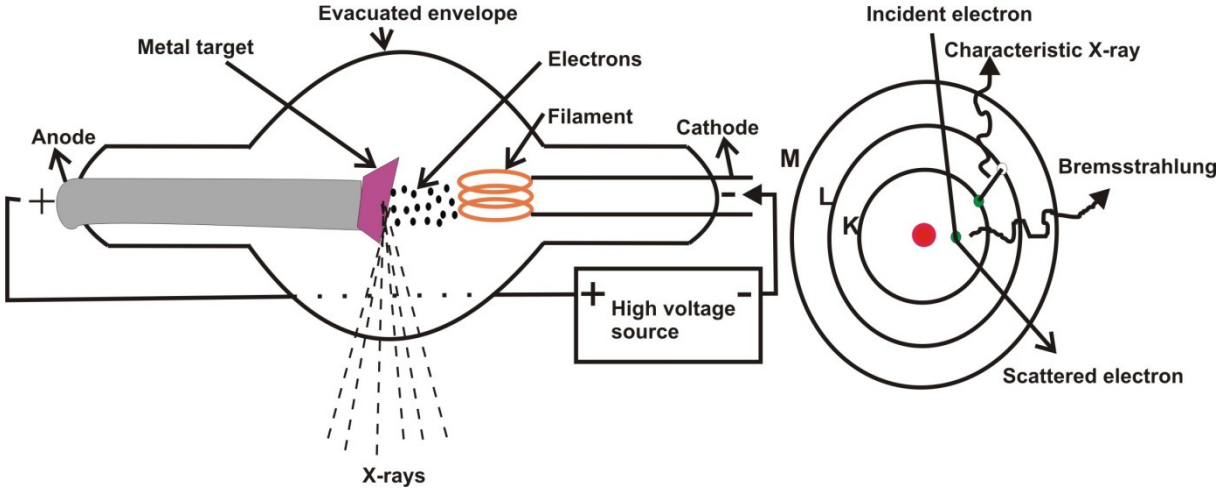

Figure 1 Left: Production of X-rays from X-ray tube. Right: process describing the emission of Bremsstrahlung and characteristic x-ray from a target metal atom.

The maximum energy of X-ray depends on the high voltage potential in between the cathode and the anode which is related as:

$$E_{max} = eV \qquad (2.2.2)$$

where, V is the accelerating voltage and e the electronic charge. The intensity of the emitted radiation can be increased by focusing the electrons beam before hitting the anode. The target material generally preferred copper, molybdenum and tungsten.

2.2.2 Synchrotron radiation

Synchrotron radiation is emitted by electron or positron travelling at relativistic speeds in applied magnetic field. Electrons (or positron) are injected in to linear accelerator (LINAC) using electron gun where electrons gain maximum energy. The energetic electrons are then injected in to synchrotron (BOOSTER) in which they circulate with nearly the speed of light. These highly energetic electrons are stored in to the storage ring and motions are due to bending the beam path by bending magnet. Thus, the accelerated electrons produce electromagnetic radiation tangentially to the storage ring as shown in fig.1. This electromagnetic radiation is called synchrotron radiation, can be decoupled and sent to experimental beamlines.

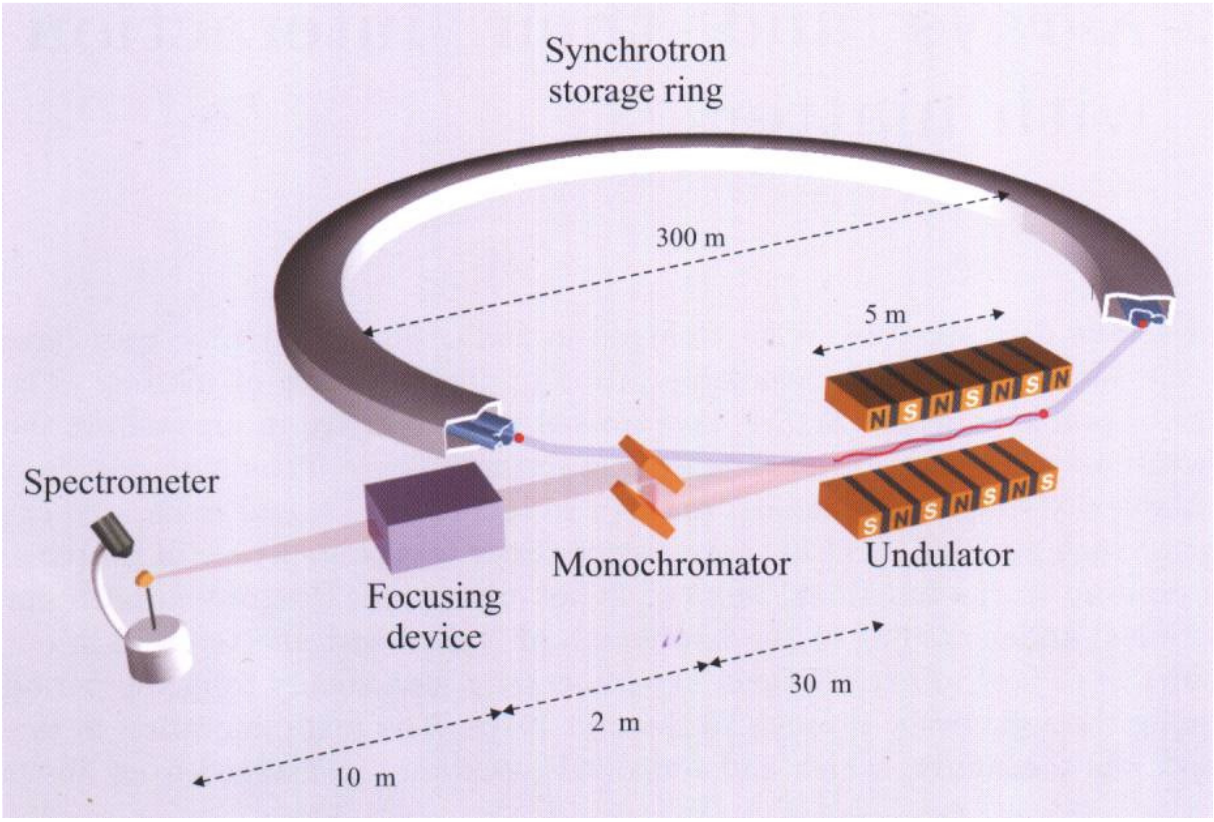

Figure 2 Scheme of Synchrotron storage ring with Undulator[17].

In addition, the insertion device is inserted in straight section of the synchrotron producing highly brilliant Synchrotron radiation more than from a bending magnet. The insertion devices are wigglers and undulators[17]. They are periodic arrangements of magnets producing deflection of the circulating beam but that forces the electron to execute transverse oscillations causing them to emit synchrotron radiation. In a wiggler the intensities of observed radiation is enhanced by a factor of 2N, where N is the number of periods. The

radiations produced in undulator are the result of the interference effect that can occur when an electron radiates in a periodic magnetic field. A necessary condition for that is the small amplitude oscillations on a scale set by γ^{-1} (where γ is the electron energy in units of the rest mass energy) and the coherent addition of amplitudes is only valid at particular wavelength. As compared to wigglers and bending magnet the radiation from undulator is highly collimated. In wigglers there are strong magnetic field i.e. fast oscillations of electrons and relativistic radiation but in undulator there is weak magnetic field i.e. slow oscillation and non-relativistic radiation. The synchrotron radiation from insertion device is treated with different optical elements and sent to the experimental hutch.Synchrotron radiation provides a continuous spectrum of electromagnetic radiation from infra-red region to hard X-ray region, with high intensity. The main properties of the synchrotron radiation are its brilliance which is defined as:

$$Brilliance = \frac{Photons/sec}{(mrad)^2(mm^2 Source\ area)(0.1\%bandwidth)}$$

It depends on the number of photons emitted per second, angular divergence of X-ray beam and size of electron beam determined by monochromator. The another property of synchrotron radiation is its brightness and is defined as[16]

$$Brightness = \frac{Photons/sec}{(mrad)^2(mA^2)(0.1\%bandwidth)}$$

Here, the normalization parameter is beam current instead of source area which is measured in mA.

In addition, it has wide energy spectrum with tunable wavelengths and highly pulsed radiation. The synchrotron radiation allows not only the better performance of conventional crystallography techniques to investigate the new materials but also facilitates major advances in different materials like polymers , superconductor and the structure of surfaces and interfaces , even at the level of single layers of molecules.

2.3 X-ray scattering from nanostructures

Scattering is one of the important interactions of X-ray with matter for structural analysis of materials. According to classical definition of X-ray scattering, the incoming wave interacts

with the electrons in matter which results to emit dipole radiation. The momentum transfer of a wave in the scattering process is:

$$q = k_f - k_i \qquad (2.3.1)$$

Where k_f and k_i are final and initial wave vectors of the waves respectively. q is the natural variable in scattering process measured in units of [nm^{-1}] or [$A^{\circ -1}$].

At sufficiently large distance R from electron and observer the emitted wave can be approximated as plane waves and the electric field of the radiated spherical wave is defined by[17]:

$$E_{rad(r,R)} = r_0 P E_0 e^{ik_i \cdot r} \frac{e^{ikR}}{R} \qquad (2.3.2)$$

Where $|k_i| = k = \frac{2\pi}{\lambda}$ and λ is the wavelength of the wave.

$r_0 = \frac{e^2}{4\pi\varepsilon_0 mc^2} = 2.82 \times 10^{-15} m$ is the Thomson scattering length,

and P is the polarization factor which depends on the scattering geometry and is expressed as:

$$P = \begin{cases} 1 & \sigma\ polarisation \\ |\cos(2\theta)| & \pi\ polarisation \\ \frac{1}{2}(1 + cos^2(2\theta)) & Unpolarised\ light \end{cases}$$

In a scattering process the different phase shift of the incoming wave occurred when it passes through different parts of object whose amplitude and phase relative to the incident wave are described by a complex scattering density ρ(r).

According to kinematical approach the total scattered amplitude A of a wave is the sum of overall scattered waves written as:

$$A_{rad}(R) = r_0 P A_0 \int \rho(r)\, e^{ik_i \cdot r} \frac{e^{ik|R'-r|}}{|R'-r|} dV \qquad (2.3.3)$$

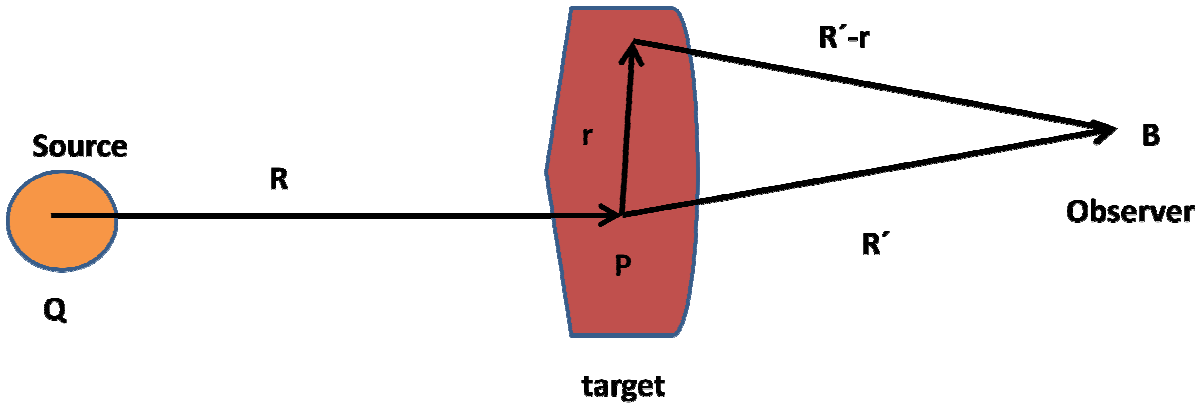

Figure 3 Schematic representation of scattering kinematics.

In Fig.3 it can be seen that the phase difference of the wave $\Delta\varphi(r)=(k_f-k_i).r=q.r$ and the volume element dv at the position r contributes an amount $r_0\rho(r)dv$ to the scattered field with a phase factor of $e^{iq.r}$. The total scattered amplitude is given by the integration of overall density distribution as:

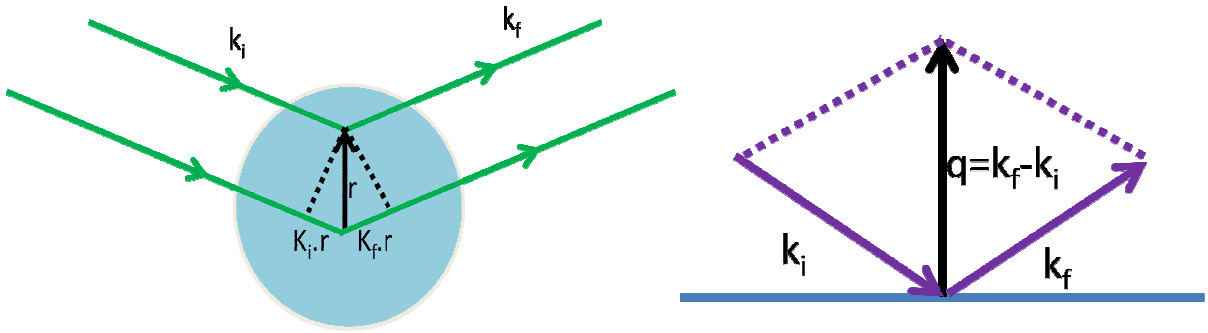

Figure 4 Left: Bragg's law. Right: The difference between the scattered and incident wave-vector defines the scattering vector q.

$$A_{rad}(R) = r_0 P A_0 \frac{e^{ik_i.r}}{R} \int \rho(r)\, e^{iq.r} dV \qquad (2.3.4)$$

In diffraction experiment for structure analysis we measure the intensity of the scattered waves but not the amplitude. Thus, scattered intensity

$$I(q) \propto \left|A_{rad(R)}\right|^2 \propto \left|\int \rho(r)\, e^{iq.r} dV\right|^2 \qquad (2.3.5)$$

The scattering intensity is the absolute square of the Fourier transform of the electron density of the scatterers. According to Fourier uncertainty principle $\Delta q.\Delta x=\pi$, we can see that the resolution of small structure requires larger q value. If we get directly the amplitude from diffraction pattern then one could make use of inverse Fourier transform to obtain the spatial

distribution of scattering density. But this is not the case; because of the lost the phase information. In order to do the particular structural analysis one propose a feasible model structure, calculate the diffraction pattern and compare it with the experimental diffraction pattern. The parameters of the model are adjusted until a best fit is obtained.

2.4 Scattering from periodic crystal[18]

It is important to analyze the scattering pattern from a periodic structure. Because the periodicity of the crystal structure is same as the periodic of the density, it can be expressed as[18]:

$$\rho(r + r_n) = \rho(r) \qquad (2.4.1)$$

Where, $r_n = n_1 a_1 + n_2 a_2 + n_3 a_3$ for integer n_1, n_2, n_3. The corresponding Fourier series in one dimension:

$$\rho(x) = \sum_n \rho_n e^{i\left(\frac{n2\pi}{a}\right)x} \qquad (2.4.2)$$

Let choose the vector G which fulfill certain conditions to preserve translation invariance of ρ with all lattice vectors. Then,

$$\rho(r) = \sum_G \rho_G e^{iG.r} \qquad (2.4.3)$$

The condition of periodicity (eqn.2.4.1) tells that,

$$G.r_n = 2\pi m \qquad (2.4.4)$$

Where m is an integer for all values of n_1, n_2, n_3. Now decompose G in to three independent basis vectors g_i,

$$G = hg_1 + kg_2 + lg_3 \qquad (2.4.5)$$

Again the condition of periodicity requires,

$$(hg_1 + kg_2 + lg_3).n_1 a_1 = 2\pi m \qquad (2.4.6)$$

The condition to satisfy this constraint for n_1 is

$$g_1 . a_1 = 2\pi\delta_{ij} \quad (2.4.7)$$

$$\delta_{ij} = \begin{cases} 1 & i = j \\ 0 & otherwise \end{cases}$$

The set of vectors (g_1, g_2, g_3) are so called basis set of reciprocal vector and defined as:

$$g_1 = 2\pi \frac{a_2 \times a_3}{a_1 . (a_2 \times a_3)} \quad \text{and cyclic permutations.} \qquad (2.4.8)$$

It shows the correspondence between real lattice and the reciprocal lattice and when this form apply for the scattering intensity formula then it becomes,

$$\text{I(q)} \propto \left| r_0 P A_0 \frac{e^{ik_i . r}}{R} \right|^2 \left| \sum_G \rho_G \int e^{i(G-q).r} \, dV \right|^2 \qquad (2.4.9)$$

The integration of the above eq. (2.4.9), for an infinite volume represents the respective δ-functions.

$$\int e^{i(G-q).r} \, dV = \begin{cases} V & for\ G = q \\ 0 & for\ otherwise \end{cases} \quad (2.5.0)$$

Therefore, the scattering from lattice leads to diffracted beam when the scattering vector q is equal to a particular lattice vector G. This is the Laue condition for diffraction.

In periodic crystal structures the constructive interference of X-ray scattered from crystal planes is described by Bragg's law[19] in fig.4 left:

$$2dsin\theta = n\lambda \quad (2.5.1)$$

Where d is the distance between the two lattice planes, θ is the incidence angle with respect to the lattice plane and n is the integer.

The length of the reciprocal lattice vector q_{hkl} is equal to 2π times the reciprocal distance between neighboring (hkl) planes.

$$q_{hkl} = \frac{2\pi}{d_{hkl}} = 2k_0 sin\theta = 4\pi sin\theta/\lambda \quad (2.5.2)$$

However, the sum of perturbation in the periodicity of the crystal structure leads to the diffuse scattered intensity around the Bragg's peaks. To analyze this intensity the total electron density ρ_{real} distribution is consider as sum of two contributions.

$$\rho_{real} = \rho_{diffuse} + \rho_{reference} \tag{2.5.3}$$

$\rho_{reference}$ is the reference crystal that leads to diffraction in the sharp Bragg's peak. The amplitude of the diffuse scattering is the

$$A_{diffuse(q)} = r_0 P A_0 \frac{e^{ik_i.r}}{R} \int \rho_{diffuse}(r) e^{iq.r} dV \tag{2.5.4}$$

This is the amplitude of the scattering wave, but in real experiment we measure only intensities. These intensities depend on how efficiently the particles in the sample scatter the radiation and is given by differential scattering cross section which is defined as normalized scattering photon flux in to an elementary solid angle dΩ

$$I(q) \sim \frac{d\sigma}{d\Omega}(q) = \frac{|A(q)|^2}{|A_0|^2} R^2 = r_0^2 P^2 \left| \int \rho(r) e^{iq.r} dV \right|^2 \tag{2.5.5}$$

2.5 Structure factor

The crystal is the combination of the crystal lattice and basis (unit cell). Structure factor accounts for the interference effect due to the wave scattered from different element of basis. The scattering condition (2.5 and 2.5.1) predicts only the position of the diffracted beam and do not give the information about intensity. The intensity of the Bragg's peak depends on the spatial distribution of atoms within the unit cell.

The scattered amplitude of the crystal is denoted by F(q) which is equal to the A(q) in previous equations and factorize in to two terms; unit cell structure factor and the lattice sum,

$$\boldsymbol{F(q)} = \overbrace{\sum_{r_j} \boldsymbol{f_j(q) e^{iq.r_j}}}^{\textbf{Unit cell structure factor}} \quad \overbrace{\sum_{r_n} \boldsymbol{e^{iqr_n}}}^{\textbf{Lattice sum}} \tag{2.5.6}$$

Where $\boldsymbol{r_j} = (\boldsymbol{x_j a_1} + \boldsymbol{y_j a_2} + \boldsymbol{z_j a_3})$the position of the atoms in unit cell is, $\boldsymbol{f_j(q)}$ is the atomic form factor of the jth atom and is expressed as;

$$f_j(q) = \sum_{j=1}^{4} a_j e^{-b_j(\frac{q}{4\pi})^2} + c = \sum_{j=1}^{4} a_j e^{-b_j(\frac{sin\theta}{\lambda})^2} + c \qquad (2.5.7)$$

Where a_j, b_j, and c are the fitting parameters[20].

Here the amplitude F(q) contains two terms, first is structure factor as function of atomic position r_j within the unit cell and the second term constitute the interference function. Thus the intensity is proportional to the square of the structure factors of the unit cell. The second term contributes to a periodic array of Dirac delta function. The intensity is non zero only if $q.a_1=2\pi h$, $q.a_2=2\pi k$, $q.a_3=2\pi l$ and q is vector of reciprocal lattice of basic vectors g_1, g_2 and g_3 which fulfills the equation (2.4.7). When the Laue condition is fulfill the intensity

$$I_{hkl} \propto \left|\sum_{r_j} f_j(q) e^{iq.r_j}\right|^2 \left|\sum_{r_n} e^{iqr_n}\right|^2 \qquad (2.5.8)$$

The structure factor in terms of the fractional atomic coordinates x_j, y_j, z_j and the atomic form factor $f_j(q)$ can be expressed by

$$S(q)_{hkl} = \sum_{r_j} f_j(q) e^{-2\pi i(hx_j+ky_j+lz_j)} \quad (2.5.9)$$

2.6 Powder diffraction

The main goal of the X-ray diffraction technique is to analyze the structure of crystalline material. The powder diffraction technique is applied for randomly oriented crystalline material. According to Bragg's law many peaks obtained in the diffraction pattern from crystalline material correspond to different crystal planes. The position of the Bragg's peak is related to the size and symmetry of the unit cell and the intensities contribution is due to the arrangement of atoms within the unit cell[21].

In case of powder diffraction the reciprocal lattice vector G_{hkl} specified by the Miller indices h,k,l are isotropically distributed over the sphere called Ewald's sphere as shown in Fig.5. The ends of identical reciprocal lattice vectors G_{hkl} on the surface of the sphere describe a circle with radius perpendicular to the incident vector k_i. The scattered wave vectors k_f aligned along cone with k_i as the axis and an apex half angle of 2θ. Basically, the diffracted intensity of scattered wave vectors on the circumference of the Debye rings is constant.

Powder diffraction

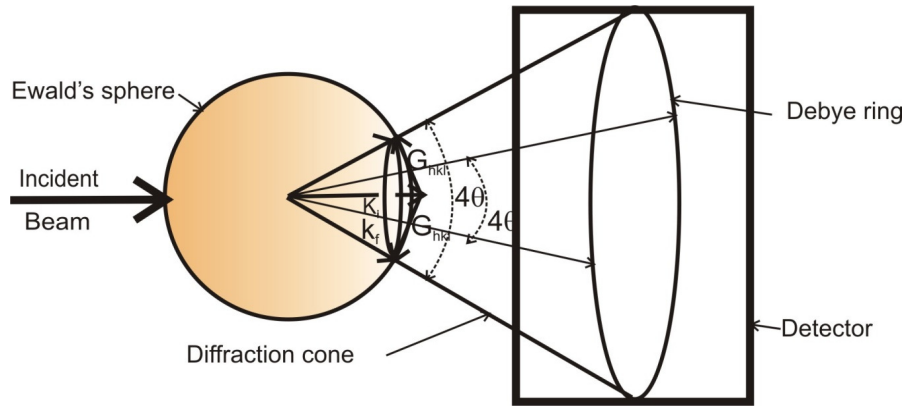

Figure 5 Powder diffraction geometry

The intensity of diffracted beam from crystalline material is measured as function of Bragg angle, 2θ. To analyze the powder diffraction data, the first step is to integrate the intensity along the ring. The intensity integration can be expressed as[22].

$$I(2\theta) = \int_{\gamma_1}^{\gamma_2} J(2\theta,\gamma)d\gamma \quad 2\theta_1 \le 2\theta \le 2\theta_2 \quad (2.6.0)$$

$$\text{Or } I(2\theta) = \sum_{\gamma_1}^{\gamma_2} J(2\theta,\gamma) \quad 2\theta_1 \le 2\theta \le 2\theta_2 \quad (2.6.1)$$

Where, $J(2\theta,\gamma)$ is the representation of intensity distribution in 2-dimensional pattern, γ_1 and γ_2 is the lower and upper limit of integration respectively. The general scheme of experimental setup in synchrotron is shown in fig.6.

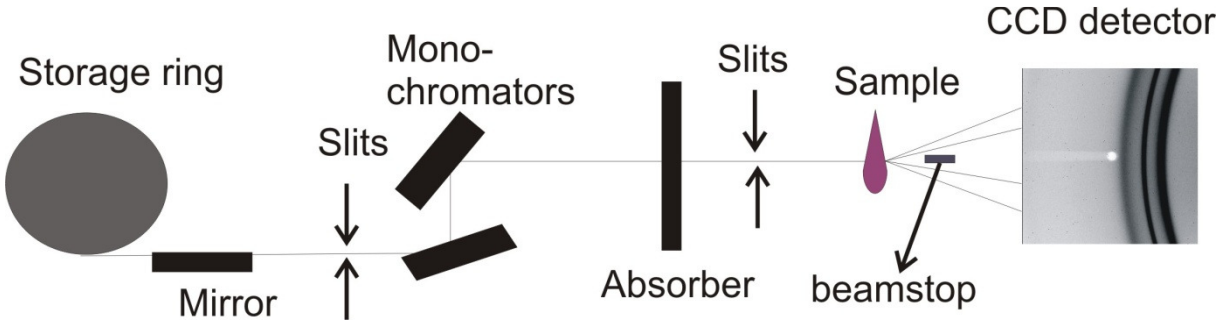

Figure 6 Schematic diagram of high resolution diffractometer at a synchrotron beamline using CCD in powder diffraction measurement[16].

A 2D diffraction frame collected with CCD detector consists of series of diffraction rings as shown in fig.7. The peaks on the right figure show the corresponding integrated intensity of the diffraction rings.

However, the q-value scale representation is choosing instead of Bragg angle representation to have a wavelength independent scale. The q-values we used for indexing and evaluation of

lattice parameters of the crystal structure. The relation between the q-space and the lattice parameter for cubic and hexagonal structure is given by[8] :

$$q = \frac{2\pi}{d_{hkl}} = \frac{2\pi}{a_{cubic}}\sqrt{h^2 + k^2 + l^2} \qquad (2.6.2)$$

$$q = \frac{2\pi}{d_{hkl}} = \frac{2\pi}{a_{hex}}\sqrt{\frac{4}{3}(h^2 + k^2 + hk) + \frac{a_{hex}^2}{c_{hex}^2}l^2} \qquad (2.6.3)$$

Where, a_{cubic} is the lattice parameter a in cubic structure, a_{hex} and c_{hex} are the lattice parameters a and c in hexagonal structure.

The scattered intensity I(hkl) of powder diffraction depends on the numerous factors like structural factors which is determined by the crystal structure, absorption factor, the multiplicity factor and θ dependent Lorenz polarization factor:

$$I_{hkl} = k\frac{M_{hkl}}{\nu^2}LPA\lambda^3 S_{hkl}^2 \exp\left(-2M_t - 2M_s\right) \qquad (2.6.4)$$

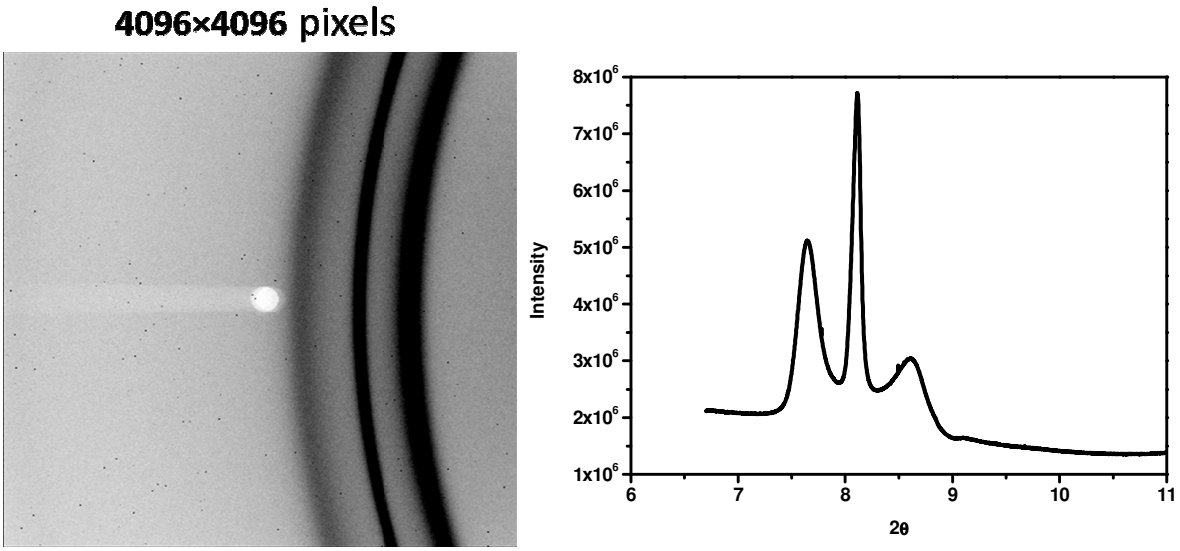

Figure 7 (Left): CCD image of CdSe-Mn nanowires measured in PETRA III DESY Hamburg, (Right): Integrated intensity from the image.

Where k is scaling factor normalize to calculated and experimentally observed intensity, ν is the volume of unit cell, λ is wavelength of x-ray and exp $(-2M_t - 2M_s)$ is a damping factor due to thermal vibrations and weak static displacement[22]. M_{hkl} is the multiplicity factor

i.e. the number of crystal planes having same atomic arrangement and d-spacing but different orientations. For cubic and hexagonal crystal system M_{hkl} is given by:

Table. 1 Multiplicity factor for hexagonal and cubic crystal system.

system	hkl	hhl	hh0	0kk	hhh	hk0	h0l	0kl	h00	0k0	00l
Cubic	48	24	12	12	8	24	24	24	6	6	6
hexagonal	24	12	6	-	-	12	12	12	6	6	2

The Lorenz-polarization factor depends on scattering angle and is expressed as.

$$LP = \frac{1+cos^2\theta}{sin^2\theta cos\theta} \quad (2.6.5)$$

The geometry and the properties of the sample affect the absorption factor. If the material has a linear absorption coefficient μ then absorption factor A is :

$$A = \frac{1}{\mu_{eff}} \quad (2.6.6)$$

For the thin material in which the incident beams easily penetrate the sample, the absorption factor;

$$A \propto 1 - \exp\left(-\frac{2\mu_{eff}t}{sin\theta}\right) \quad (2.6.7)$$

Where, $\mu_{eff}$is the effective linear absorption coefficient and t is the thickness of the sample.

The Debye-Waller factor contains two terms, the first one is $\exp(-2M_t)$ is called Debye temperature factor and is written as:

$$M_t = B_t\left(\frac{sin\theta}{\lambda}\right)^2 \quad (2.6.8)$$

With $B_t = 8\pi^2\langle\mu_t^2\rangle$. where, $\langle\mu_t^2\rangle$ is the mean displacement due to thermal vibration. The attenuation factor increases by increasing the temperature. The second term $\exp(-2M_s)$ is due to weak static displacement and given as.

$$M_s = B_s\left(\frac{sin\theta}{\lambda}\right)^2 \quad (2.6.9)$$

With $B_t = 8\pi^2\langle\mu_s^2\rangle$. where, $\langle\mu_s^2\rangle$ is the mean square displacement of the static distortion normal to the diffracting planes. This displacement is caused by the defects in the crystal such as stacking faults, doping etc. It can be ignored in most of the powder diffraction experiment.

The main factor which depends on the intensity is the structure factor S_{hkl}. The integrated intensity in the diffraction (hkl) peak is proportional to $|S_{hkl}|^2$ and is given by

$$|S_{hkl}|^2 = S_{hkl}.S_{hkl}^* \quad (2.7.0)$$

Where, S_{hkl}^* is the complex conjugate of S_{hkl}.

Chapter 3

3. Simulation of CdSe nanowires

Due to the very small size of the nanomaterial, it is difficult to obtain precise structural information. Therefore, the simulation of nanomaterial became a powerful tool to predict the structural information as well as other properties. Experimentally, X-ray powder diffraction technique is used to analyze the size, shape and structural quality of nanoparticle[23]. Here we present the simulation of CdSe NWs using the software package DISCUS. The program is used to simulate the crystal structure, with or without defects. The introduction of a shape function enables to calculate the powder diffraction pattern or PDF. Different macros files and command language that is based on the FORTRAN is used to run the program. More details of this program is found in textbook of "Diffuse Scattering and Defect Structure Simulations" by R.B.Neder and T.Proffen[24]. DISCUS is developed for spherical nanoparticles and it is applied here for simulation of randomly oriented NWs.

For the simulation of nanoparticle, a few parameters and the co-ordinates of the atoms are defined in order to create the structure. To refine all structural parameters, an evolutionary algorithm[25] based on the differential evolutionary approach[26], which is more convenient for nanoparticle simulation is used in the program. The XRD pattern of CdSe Nws shows that it crystallizes in the Wz or ZB structure; the NWs are simulated by stacking layers of these structures with a given stacking probability. Generally the simulation of CdSe NWs is executing four steps: creation of ZB/Wz type layers; Stacking of these layers; creating the shape of NWs; calculation of powder pattern. All the macros files that are used to create CdSe Nws and calculate powder diffraction pattern are given in Appendix.

3.1 Creation of Wurtzite/Zincblende layers

The Wz or ZB structure can be described as hexagonal or cubic close packed structures of the selenium/cadmium with half the tetrahedral voids filled by the cadmium/selenium. To make the simulation easy it is better to create double layers, one closed packed Cd layer and one closed packed Se layer which are identical for both structures. In ZB structure these double layers are stacked in ABCABC….sequence while in Wz structure the stacking sequence is ABAB…… and the B layer is rotated around the c-axis by 180°. For ideal Wz structure the position of Se and Cd atoms are:

Se	1/3, 1/3,	2/3, ½	0	and	2/3,
Cd	1/3, 1/3,	2/3, 7/8	3/8	and	2/3,

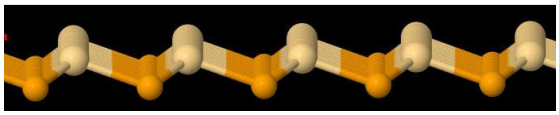

Figure 8 Double layer created in CdSe NWs: upper layer is closed packed Cd layer and lower is closed packed Se layer.

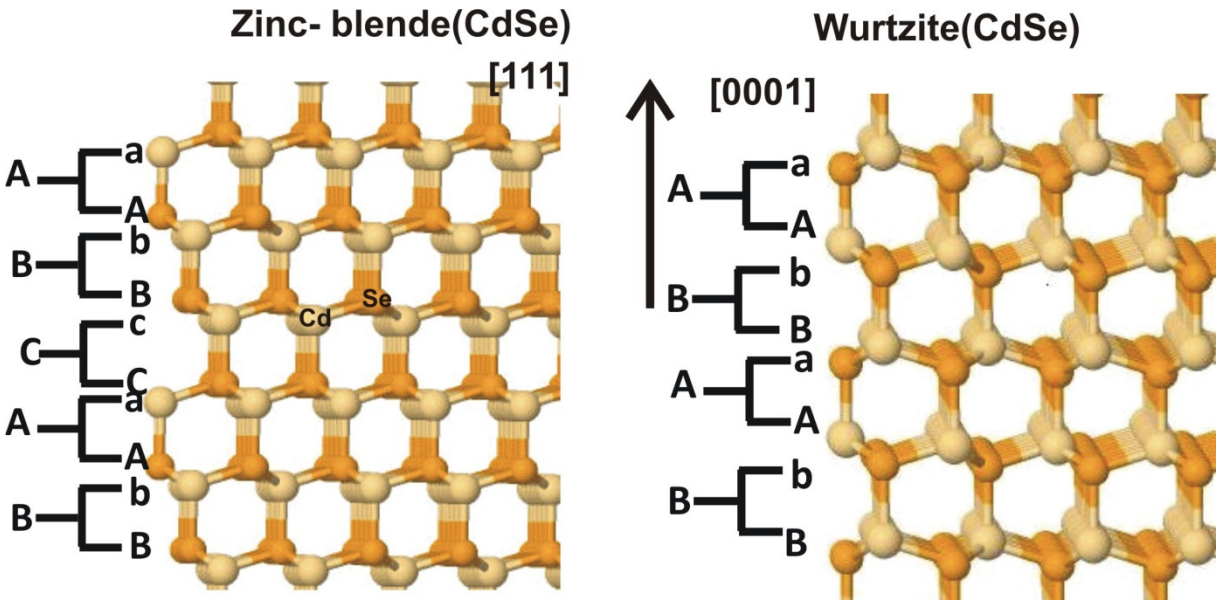

Figure 9 Relative positions of different layers in ZB and W structure of CdSe NWs created from the simulation.

A double layer could be the pair of Se, Cd atoms at 1/3, 2/3, 0 and 1/3, 2/3, 3/8. Each layer has hexagonal symmetry, the vectors from an A layer to B layer are [1/3, 2/3, ½], and their symmetrically equivalent vectors [1/3, -1/3, ½] and [-2/3, 1/3, ½]. Similarly, the vectors from A layer to C layer are [2/3, 1/3, ½], or [-1/3, 1/3, ½] or [-1/3, -2/3, 1/2]. In our simulation we usually use the pair AB: [1/3, -1/3, ½] and AC: [-1/3, 1/3, ½]. The ZB structure is formed

when the double layers are always stacked with the vector [1/3, -1/3, ½] while the Wz structure formed using alternating the interlayer vectors [1/3, -1/3, ½] and [-1/3, 1/3, ½].

To minimize the computational effort, the appropriate size of the layer is calculated from the side plane along the radius of the NW. For cylindrical NWs the required number of unit cells can be calculated as the integer part of 4.5*radius/a, where 'a' is the lattice constant. Similarly, the number of layers required is calculated from the height of the NWs. In case of Wz structure, there are two Wz layers per unit cell therefore total number of layers in the NW is 2*height/c, where c is the lattice constant. The macro file which creates the layer is "makelayers.CdSe" is given in appendix.

3.2 Creating structures with stacking faults

The phenomenon of formation of stacking faults occurred during the time of crystal growth or by mechanical deformation of an as grown crystal. This type of defect often observed in crystals and commonly found in hexagonal and cubic closed packing structure is built up from layer like structural units[24]. The deviation from the periodic sequence along the stacking direction normal to the layers is defined by stacking faults (growth fault and deformation fault). For simulation of stacking faults, the parameters are defined considering the following aspects: types of layers, translation vector from one layer to another layer, the probability at which one layer type is stacked with other layer with a given translation vector, and the type and position of current layer is determined by the type of n previous layer.

3.2.1 Growth fault

In growth fault, the deviation occurred in ideal periodic sequence ABABAB….in hexagonal closed packed (hcp) and ABCABCABC…. in cubic closed packed. It is observed ABACABAB… in hcp and ABAC… sequence in cubic closed packed structure but ABBA cannot occur. To create the CdSe Nws with growth faults, layers are added one by one to an existing NW. One dimensional Markov chains[24, 27] describe the process of adding different types of layer. The one dimensional lattice is expressed by binary (0, 1) random variables x_i; where x_i =1 denotes that site i is occupied by an A type layer and x_i =0 by a B type layer. There are three different layer positions, A, B, and C in closed packed structures but only two states is enough for the random growth faults. In this case, these states would

corresponds to a vector between adjacent layers of A = [1/3, -1/3, ½] and B = [-1/3, 1/3, ½], rather than absolute position of an individual layer. The probability of adding by A-type layer at site i may be written as:

$$P(\mathrm{x_i} = \mathrm{A}|\mathrm{x_{i-1}}) = \alpha + \beta \mathrm{x_{i-1}} \qquad (3.2.1)$$

Where α and β are parameters that determine the pair probabilities. For α=1 and β=-1, the probability of AA pair is zero and that of AB pair is 1, for α=0 and β=1, the probability of AA pair is 1. Therefore, first set of parameters create periodic sequence ABABAB…. while second set of parameters create AAA….sequence. The type of layer A and B corresponds to a vector between adjacent layers, the first sequence formed the hcp structure while second form cubic closed packed.

The parameters α and β are related to the fraction of A type layer and the pair correlation coefficient as:

$$m_A = \alpha/(1-\beta) \qquad (3.2.2)$$

$$C = \beta \qquad (3.2.3)$$

$$\alpha = m_A(1-\beta) = m_A(1-C) \qquad (3.2.4)$$

Alternatively, the probabilities of pairs in the form of a matrix can be written as:

$$\begin{pmatrix} P_{AA} & P_{AB} \\ P_{BA} & P_{BB} \end{pmatrix} = \begin{pmatrix} \alpha+\beta & 1-\alpha-\beta \\ \alpha & 1-\alpha \end{pmatrix} \qquad (3.2.5)$$

The matrix (3.2.5) is used to stacking Wz/ZB layers by simulation. From above condition it is clear that if:

$$\begin{Bmatrix} P_{AA} = 0; \ purely\ hexagonal\ closed\ packed\ structure \\ P_{AA} = 1; \qquad purly\ cubic\ closed\ packed\ structure \\ P_{AA} = x; \ where \quad 0 < x < 1; \qquad mixed\ structure \end{Bmatrix} \qquad (3.2.6)$$

3.2.2 Deformation faults in nanocrystal

When one part of the crystal is shifted parallel to the previous layers with respect to the other part deformation faults occurred. In closed packed structures, the shift is equivalent to the projection of the ordinary interlayer vector [1/3, -1/3, ½] in to the ab-plane. For the ab-plane this vector become ±[1/3, -1/3, 0] and its symmetrically equivalent vectors are ±[1/3, 2/3, 0] and ±[2/3, 1/3, 0] . Each vector shifts an A layer into a B layer or C layer and correspondingly shifts a B layer or C. The layer shift in such a way change the hexagonal closed packed structure as shown below:

....A B A B A B A B A B A B... **....A B A B A B C A C A C...**

.... h h h h h h h h h h h h... **....h h h h h c c h h h h...**

This is due to the shift of all layers on the right along the shift vector [-1/3, 1/3, 0]. In cubic closed packed structure the periodic sequence changes from left to the right as shown below.

...A B C A B C A B C A B C... ...A B C A B C B C A B C A B...
...c c c c c c c c c c c c c ...c c c c c h h c c c c c c ....

In sixth and seventh layer the direction of interlayer vector changes and then returns to the same stacking sequence before the faults. It can also be considered as the special type of growth fault.

For the simulation the layers are stacked according to stacking fault probability. Cylindrical boundary conditions we used to make the NW, where all atoms outside the cylinder are removed.

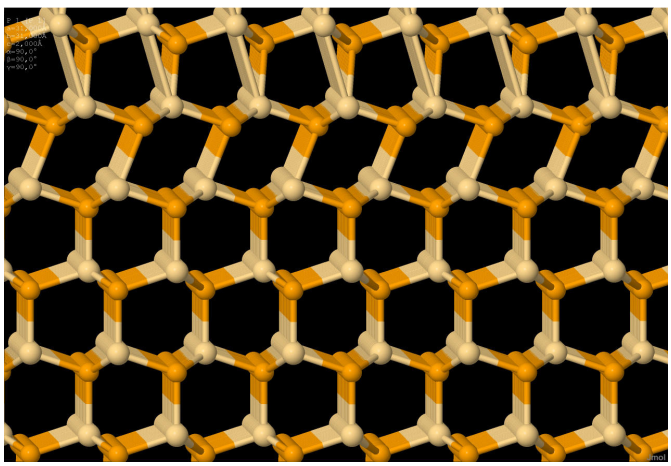

Figure 10 Part of the CdSe NW shows the deformation faults in upper three double layers.

3.3 Powder diffraction from CdSe nanowires

In principle, a powder diffraction pattern is the spherical average of diffracted intensity from a group of atoms. Debye equation is the perfect tool to evaluate the diffracted intensity under the first Born, or kinematic approximation. The powder diffraction pattern in DISCUS program can be calculated according to the Debye formula[28, 29].

$$I(q) = \sum_m f_m^2 + \sum_m \sum_{n;m\neq n} f_m f_n \frac{\sin(qr_{mn})}{qr_{mn}} \quad (3.3.1)$$

Where f_m and f_n are atomic form factor of the atoms m and n as a function of q=4πsinθ/λ, and r_{mn} is the interatomic distance. The first sum runs over all atoms m in the structure of nanowire, the second sum runs over all pairs of different atoms, i.e. $m \neq n$. Each pair of atoms contributes by a sine wave to the intensity $I(q)$. The calculation of intensity becomes faster if the crystal is transformed into Cartesian space prior to the calculation of the powder pattern.

Generally in powder diffraction, the stacking fault parameters are introduced in a random process. Each of the simulated NW has slightly different diffraction pattern due to the presence of stacking fault in different positions. This needs to create the powder pattern of several NWs.

However, there is no definite number for the average but it depends on the stacking fault parameters. If the stacking parameter is close to zero i.e. perfect crystal, it can be simulated each time. For the high number of stacking faults the number of possible configuration increases and acquires to take the average of many particles in to account. In order to do so, we need to determine how much the intensity varies from one simulation to another. To estimate the required number of NWs, it is necessary to simulate fairly large numbers (50). Then take the average intensity of these Nws e.g. 5, 10, 15, 20, 25, 30, 35, 40, 45, 50 separately and compare it. There is small deviation of intensity for the average intensity of 5 and average intensity of 10 NWS but after certain number the intensity becomes constant. For example the average intensity of 20 NWs, 25NWs, 30 NWs, 35NWs, …, are same then the selected number to take the average is 20 or more than 20.

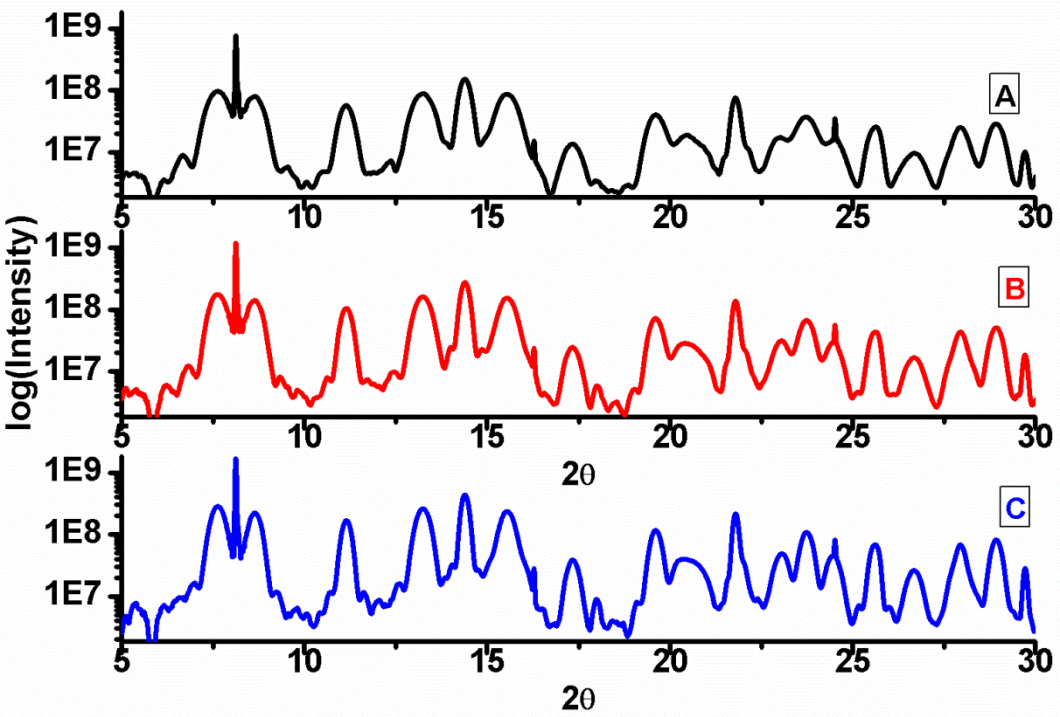

Figure 11 Size dependent diffraction patterns of simulated CdSe NW.

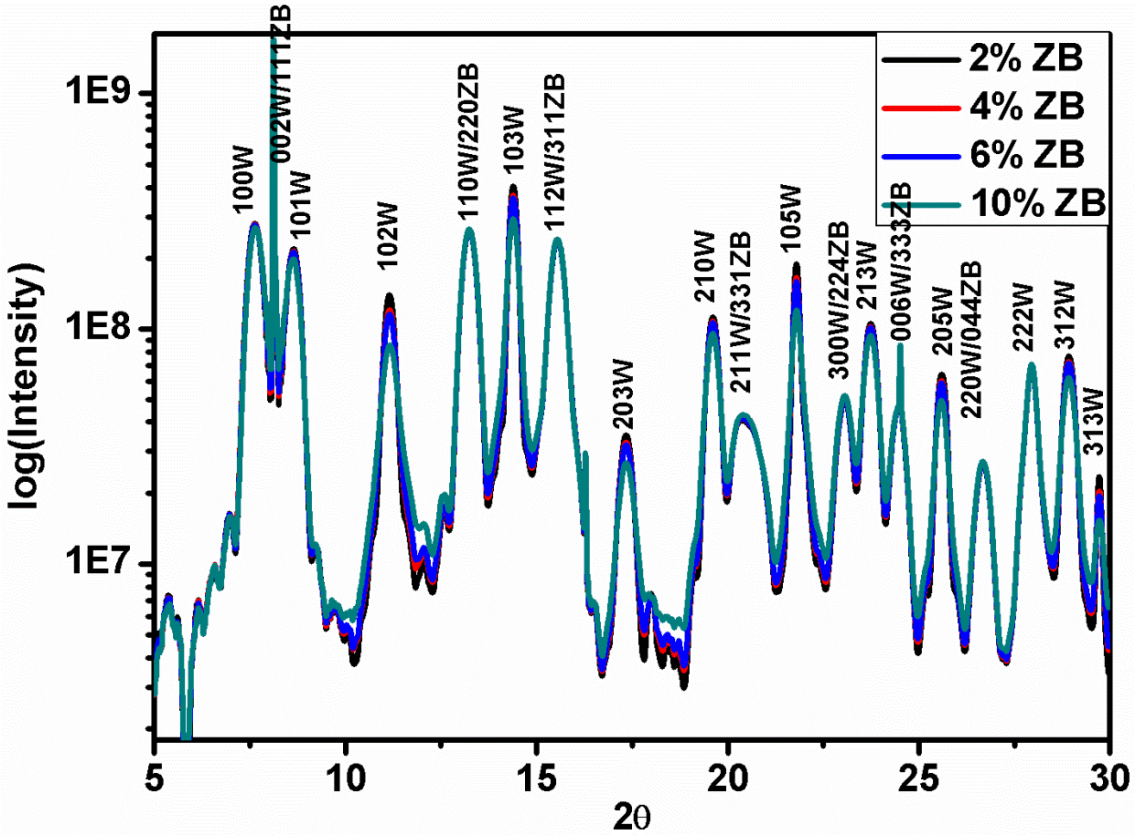

Figure 12 Powder diffraction patterns of simulated wurtzite/ZB CdSe NWs.

Figure 11 shows the powder diffraction pattern of CdSe NWs with pure wurtzite structure having different diameters (A=4nm, B=5nm, C=6nm) and constant length (60nm). The wavelength used for the X-ray pattern is 0.496A°. Each of the patterns is taken as the average diffraction pattern of 20 NWs. It is clearly seen that, the increase in diameter of the NW increases the intensity of the pattern. There is no peak shift that depends on size but the full width half maxima (FWHM) of peaks decreases with increases the diameters of the NWs.

The powder diffraction pattern of simulated polytype crystal structures of CdSe NWs is shown in fig.12 where the contribution of ZB to Wz in NW was varied. Each pattern is from the same size (6nm diameter and 60nm length) and shape of the NWs. The average was taken from 30 NWs for each pattern. Pattern demonstrates that by increasing the ZB content, the intensity decreases in pure Wz reflections. The FWHM also increases by increasing the ZB stacking; however the intensity is not affected in reflections which appear in ZB and in Wz also. The pure Wz peaks 103Wz, 203W, 105Wz, 205W, 313W are more affected rather than other Wz peaks due to ZB units in NW.

Another example for the simulation of random stacking faults is shown in fig.13. All three patterns consider the same size (6nm diameter and 60nm length) of CdSe NW but includes a different percentage (5%, 10% and 15%) of random stacking faults. The effect of deformation faults are observed clearly in the diffraction pattern by increasing the stacking fault parameter. Each simulated diffraction pattern is the average of 30 CdSe NW powder patterns.

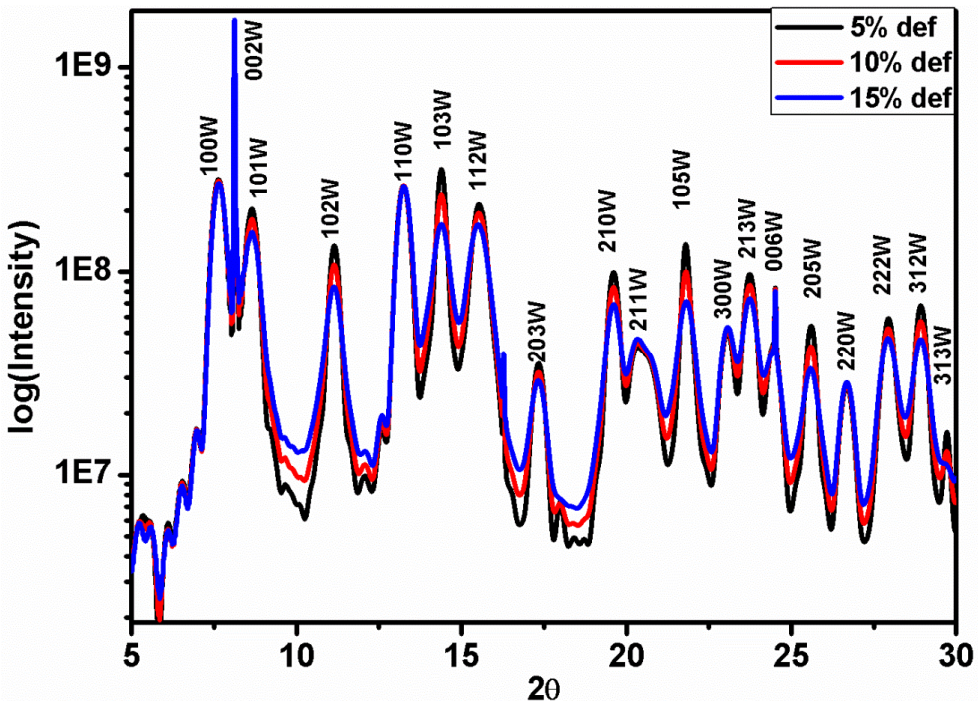

Figure 13 Simulated diffraction diagram of random stacking faults present CdSe NWs.

By increasing the probability of random stacking fault systematically, the intensity and the FWHM of certain reflections increase linearly. The position of the reflections does not shift due to the influence of stacking fault. The simulation of CdSe NW clearly shows, the peak broadening effects are more influenced for the reflections 103W, 203W, 105W, 205W than other reflections. It is also observed for the peaks 100W, 002W, 110W, 300W, 006W, 220W are independent of faults.

3.4 Doping in CdSe nanowire

Intentional doping of CdSe NWs is either replacement of Cd^{+2} ion by another dopant ion or incorporation of interstitial sites of the CdSe structure. For example in manganese doped CdSe NWs Mn^{+2} ions is replacing by Cd^{+2} ions. Since the Mn^{+2} ion is slightly smaller than the Cd^{+2} ion it leads to the change in the energy of the crystal lattice causes structural disorder. This disorder is caused by the relaxations of atoms around a vacancy. Lennard-Jones potential can be used in Monte-Carlo (MC) simulations to create displacement disorder. The energy of the Lenard-Jones potential is given by[30, 31]:

$$E_{lj} = \sum_m \sum_{n \neq m} D \left[\left(\frac{\tau_{mn}}{d_{mn}}\right)^{12} - 2\left(\frac{\tau_{mn}}{d_{mn}}\right)^{6} \right] \qquad (3.4.1)$$

The sums are over all sites *m* within the crystal and all neighbors *n* around site *m*, d_{mn} is the distance between the neighboring atoms or molecules, τ_{mn} is the distance where Lennard-Jones has it potential minimum and from the potential depth D has negative value.

The MC simulation is a statistical simulation method to describe the sequence of random variables. It is used in simulation to minimize the energy of disordered variables [24, 27, 32]. The MC algorithm which is used in the simulation is shown in fig.14.

The occupancies of displacements of randomly distributed variables in an average structure can be expressed by its total energy E. In the model structure, the variables are changed randomly by random amount. The energy difference ΔE of each step is computed before and after the variable is changed. A new configuration can occur with a probability given by Boltzmann partition,

$$P_{config} = \frac{\exp\left(-\frac{\Delta E}{KT}\right)}{1+\exp\left(-\frac{\Delta E}{KT}\right)} \qquad (3.4.2)$$

Where, k is Boltzmann constant and T is temperature. The probability of random variable can be chosen in the range [0, 1].

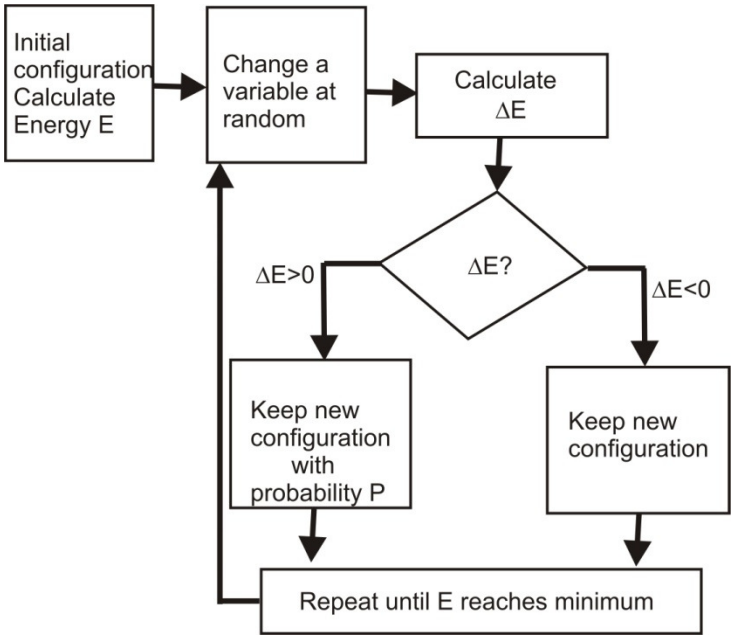

Figure 14 Schematic diagram of MC algorithm.

One example of simulated powder diffraction pattern of Mn doped CdSe NW is shown fig.15. In simulation Mn atoms are replacing Cd atoms using a nearest neighbor distance chosen

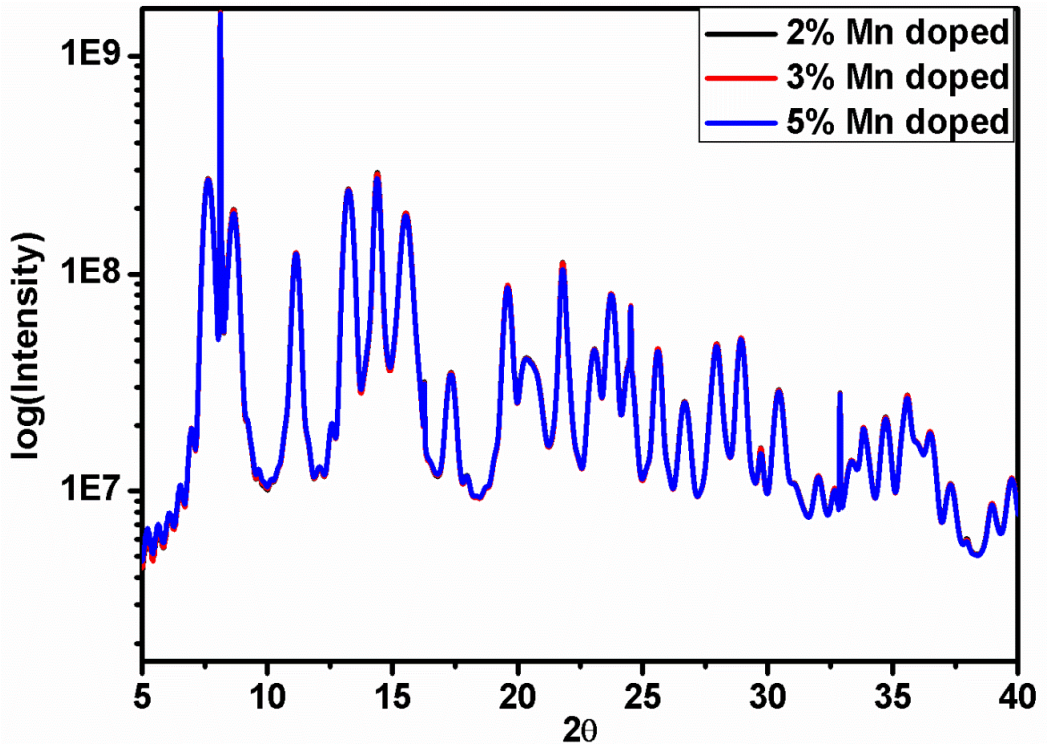

Figure 15 Simulated powder diffraction pattern of Mn doped CdSe NWs.

between Cd-Se and Mn-Se. The MC cycle creates a local distortion using different Lennard-Jones potentials for Cd-Se and Mn-Se. Due to the smaller electron number of Mn (25) compared to Cd (48), the X-ray intensity is slightly decreasing by increasing the doping concentration. However, the effect is seen to be very low because the creation of local distortions using MC cycle did not work properly in the program. Therefore, the effect of changing intensity caused by doping is excluded during further consideration.

Chapter 4

4. Sample preparation and experimental techniques

4.1 Sample preparation techniques

The synthesis of 1D nanostructure is described by different growth mechanisms such as Vapor Liquid Solid (VLS) method, Molecular-Beam-Epitaxy (MBE) method, Solution-Liquid-Solid (SLS) method. However, SLS method used to prepare the samples for present investigation is described below.

4.2 Solution-liquid-solid (SLS) method

The Solution-Liquid-Solid (SLS) method is a synthetic method for semiconductor NWs. It is a solution based catalyzed growth mechanism in which a nano-metallic catalyst is used to decompose of metallo-organic precursors for crystalline NW growth[33, 34]. The SLS method may have an advantage in providing NWs with smaller diameter that exhibit stronger quantum-confinement effects (typically<10nm), high crystallinity and surface passivation[33, 35].

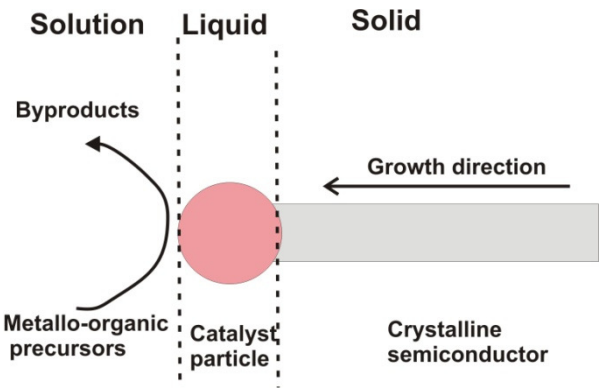

Figure 16 Schematic diagram of SLS mechanism for semiconductor NW growth.

The Cdse NWs prepared by this method uses liquid Bi nanocatalyst to synthesize the solid NWs: solution via liquid to solid. The nanowire is suspended in a organic compound thus called colloidal NWs. The main advantage of such NWs is to be relatively inexpensive for device fabrication. The details for the growth mechanisms are found in Refs.[9 and 12].

The general procedure of Mn doped CdSe NWs is described in the following, a summary of the reaction parameter of undoped and Fe, Co doped samples are shown in table[1]. The Mn doped CdSe NWs were synthesized using MnSe nanoclusters as a precursor. To prepare the MnSe nanocluster solution firstly 2.45g manganese stearate was dissolved in 20 mL octylether in the presence of 2.0 mL TOP(trioctylphosphine) and then mixed with 2.0 mL TOPSe (2.0 mol/L). The reaction of the mixture took place 3h at 100°C under a vacuum (1mba). The colourless solution gradually turned into brown, indicating the formation of MnSe nanoclusters. Then the flask was filled with Ar and the temperature was increased to 150°C and keep for 1h. The MnSe cluster solution was cooled down and stored in glove box (H_2O<1ppm) for use.

Further, 3.0g TOPO, 24.7mg CdO and 0.23mL octanoic acid were loaded in a 50-mL three necked flask connected with a reflux condenser and a standard Schlenk line. The mixture was dried and degassed for 30min. at 100°C under a vacuum. After the flask was filled back with Ar, the temperature was increased to 330°C to result in clear solution and keep reaction for 30 min. Then a mixture of Bi nanoparticles (100 μL, 3.63 mM) and 0.5 mL as synthesized MnSe solution was quickly injected into Cd-precursor solution at 330°C.

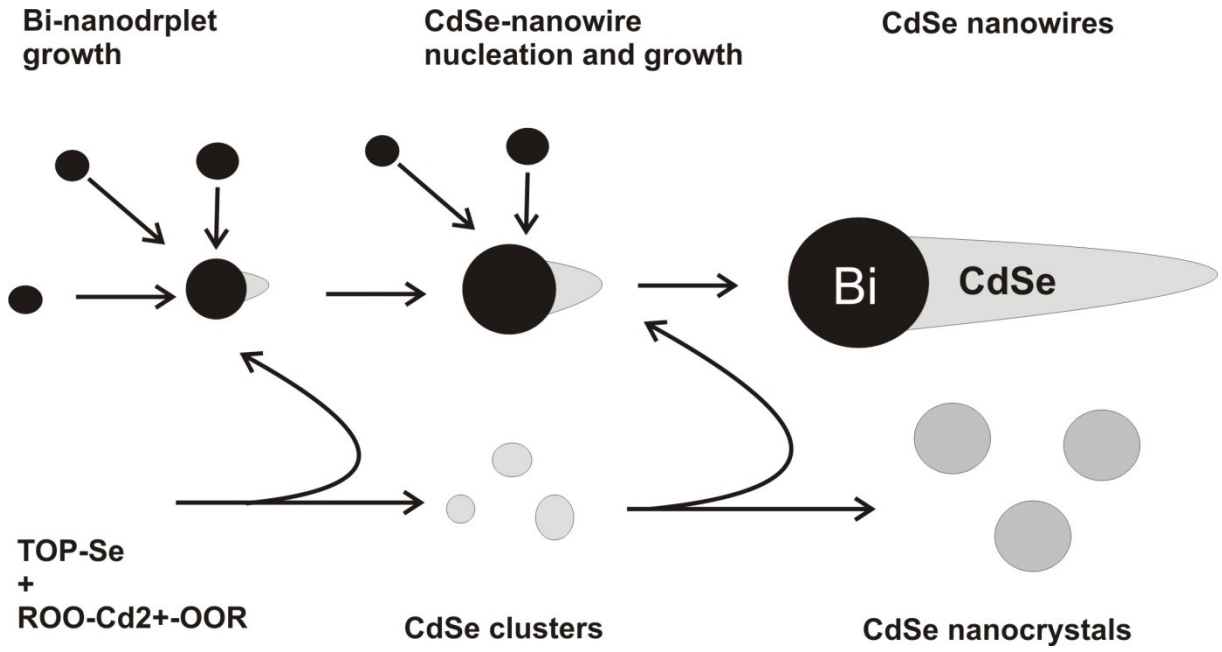

Figure 17 Growth process of one-dimensional CdSe nanowires.

The solution reacted for 1 min. and then cooled down to 80°C, followed by the addition of 2 mL toluene to prevent the TOPO from solidifying. The resultant NWs were separated from solution through high speed centrifugation (14800 rpm, 10 min.) and washed with toluene for several times. The purified nanowires were re-dispersed in chloroform for characterization.

The growth process of CdSe nanowire through SLS process is shown in fig. 17(adapted from reference [9]). When we mix the solution of CdO and the Selenium precursor along with the Bi nanocatalyst and inject there at high temperatures, large Bi nanodroplets are formed. These react with the Cd and Se precursors and start the growth of CdSe nanowires. The CdSe nanowires is extend in lengths depending on the reaction conditions like temperature, ratio of Cd and Se precursor, nanocatalyst volume, and growth time. The synthesized doped NWs are represented by the symbols 0.25Mn-CdSe, 1Mn-CdSe, and 2Mn-CdSe corresponding to the amount of MnSe cluster solution used. For 0.25Mn-CdSe NWS 0.25 mL of MnSe solution, 1Mn-CdSe NWs 1mL of MnSe solution and 2Mn-CdSe NWs 2mL of MnSe solution we used respectively.

4.3 SLS growth of CdSe nanowires.

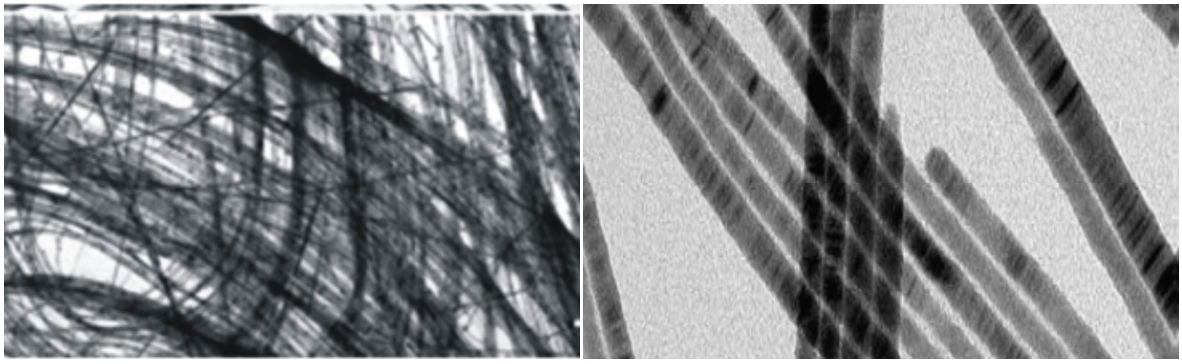

Figure 18 Left:- TEM images of CdSe NWs synthesized from SLS method; Right:- enlarged image of CdSe NWs.

The NWs synthesized from SLS method are variable in diameters and lengths depending on the parameters used in the chemical reaction and the reaction conditions. Because of the very thin diameter (few nm) and long NWs (few μm), it forms some texture like structure seen in fig. 18. In such structures parts of many NWs are overlapping each other which may create some more structural defects rather than separate parts of NWs at the time of growth process.

4.4 Sample information

The Mn-doped Nws synthesized as described above are randomly oriented with diameters varies between 8-19 nm determined from the TEM images show in Figure 19.

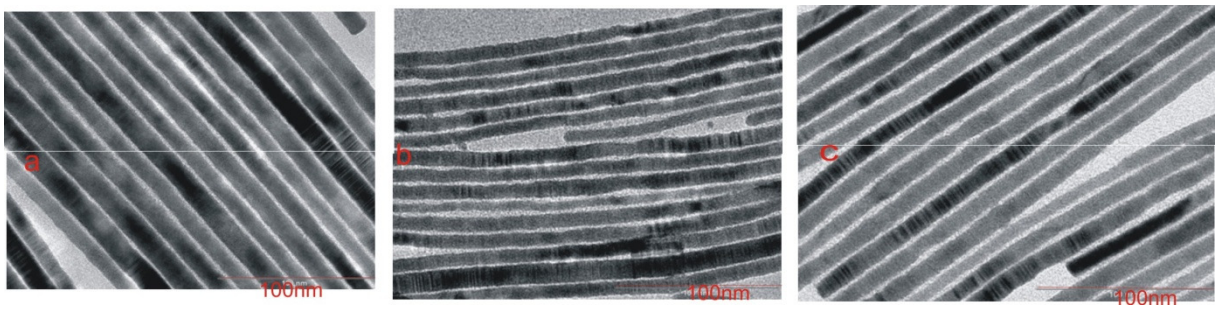

Figure 19 TEM images of NWs; a) 0.25Mn-CdSe, b) 1mn-CdSe, c) 2Mn-CdSe.

The average diameter of Mn-doped CdSe NWs samples we estimated from TEM images, they are 12.2±2 nm, 8.3±1.1 nm, and 10.1±1.3 nm for the sample a, b and c. The TEM images shows that NWs have rather uniform thicknesses and smooth surfaces along the growth direction. The different brightness along the same NW indicates the changes in the orientation or other structural changes[8, 36]. Here we expect two crystalline phases (Wz and ZB) that contain some stacking faults. The white straight line seen in fig.19 'a' and 'c' is connection between two images. The preparative parameters for different samples are summarized in table 2.

Table. 2 Preparative parameters of undoped, Co-doped and Fe-doped CdSe nanowires.

Sample	CdO (mg)	TOPO (g)	OCA (µL)[a]	TOPSe (µL)[b]	$CoSt_2$ (mL)[c]	$FeSt_2$ (mL)[d]	Bi (µL)[e]	T (°C)	t (s)
1	24.4	3.02	230	100[f]	---	---	100	330	**30**
2	24.8	3.16	230	100[f]	0.25	---	100	330	**60**
3	24.8	3.06	230	100[f]	0.50	---	100	330	**60**
4	25.1	3.05	230	100[f]	1.0	---	100	330	**60**
5	24.6	3.04	230	100	---	0.25	100	330	**60**
6	25.4	3.14	230	100	---	0.50	100	330	**60**
7	**24.7**	**3.14**	**230**	**100**	**---**	**1.0**	**100**	**330**	**60**

[a] OCA: octanoic acid; [b] TOPSe concentration is 2.0 M; [c] $CoSt_2$ concentration is 41.8 mg/mL ;[d] $FeSt_2$ concentration is 25 mg/mL ;[e] Bi concentration c_{Bi} = 3.63 mM; t is growth time.

4.5 Experimental setup and measurements

Structure investigations at the synthesized CdSe NWs are performed as X-ray powder scans. For this purpose the measurements were performed either at PETRA III beamline P08 or at DELTA beamline BL9. PETRA III provides highly brilliant synchrotron radiation. We characterize our CdSe NWs samples in high angular resolution diffraction at beamline P08 using a point detector and CCD detector. The selected energy for the point detector is 8.8 KeV (wavelength 0.66A°) and for the CCD detector is 25KeV (wavelength 0.496A°) respectively. The size of CCD detector is 4096*4096 pixels with pixel size of 15µm and beam size is 1mm*500µm (horizontal*vertical).

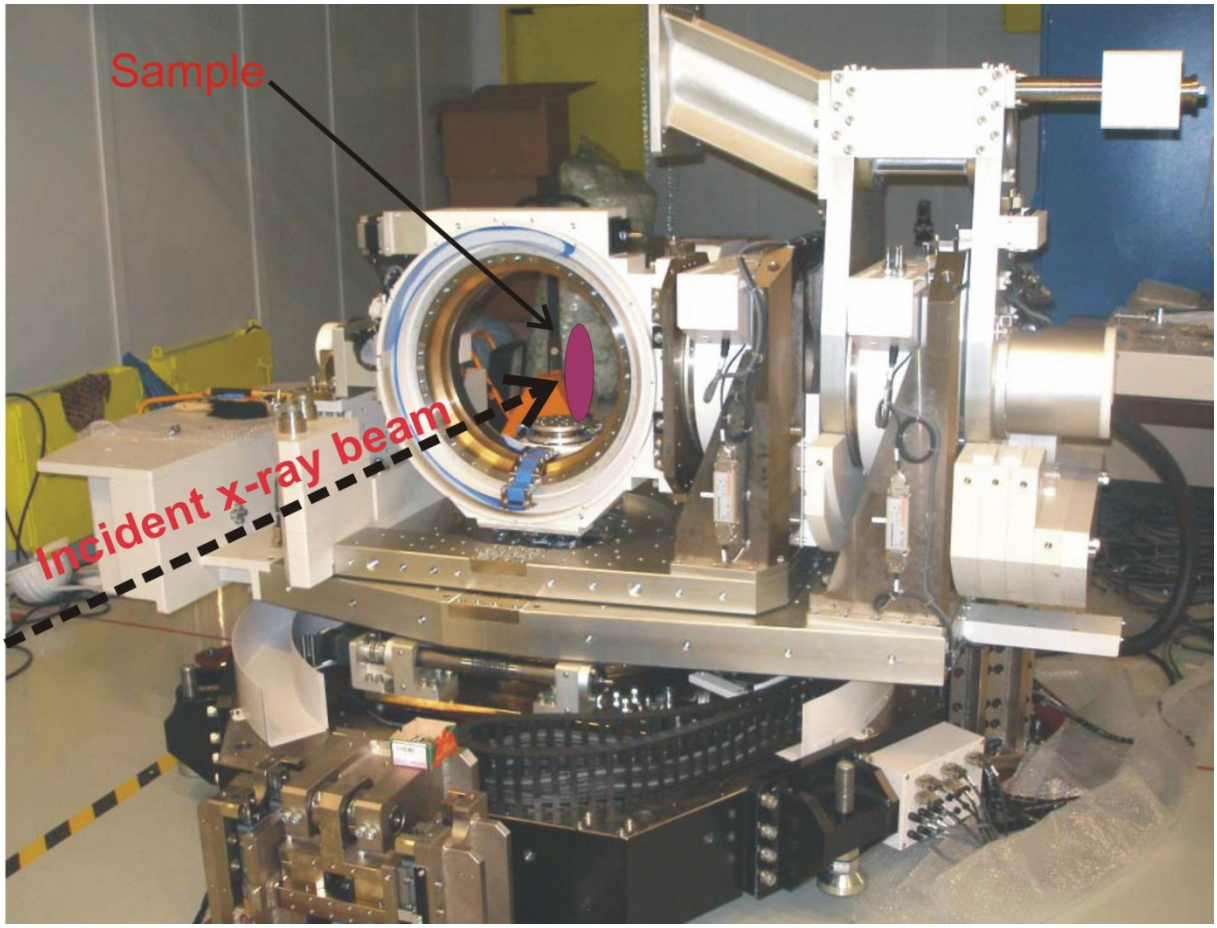

Figure 20 The high precision 6-circle diffractometer in PETRA III P08 beamline.

For powder diffraction measurement the samples of CdSe NWs are loaded in between two capton foils and are mounted it in the Kohzu high precision 6-circle diffractometer. The experimental hutch of PETRA III P08 beamline is shown in fig.20. The experiment is done with transmission diffraction geometry. The distance between the sample and the CCD detector was taken as 77cm. Diffracted intensities of the sample form Debye rings on the CCD as shown in fig.7. In CCD detector the sensitivity of individual pixel is not constant

therefore one pixel may look darker than its neighbored pixel even of the same amount of light hits both. This is explained by different noise level of the respective pixel. To correct for this effect each pixel is normalized by the average intensity of the flat field. This smoothes image and helps to correct the error from background.

Similarly, in DELTA we used synchrotron radiation of 15.5KeV photon energy with corresponding wavelength 0.799A° and beam size of the radiation was 1×1 mm^2. In experiment an image plate detector was used and the distance between the sample and detector was adjusted to cover large scattering angles (2θ) as possible. In image plate detector, a ring like scattering pattern of uniform intensity was obtained which was radially averaged using Fit2D software[37] as shown in fig.21. The data are calibrated with respect to the distance and the beam centre position x and y was found using silicon powder as reference material.

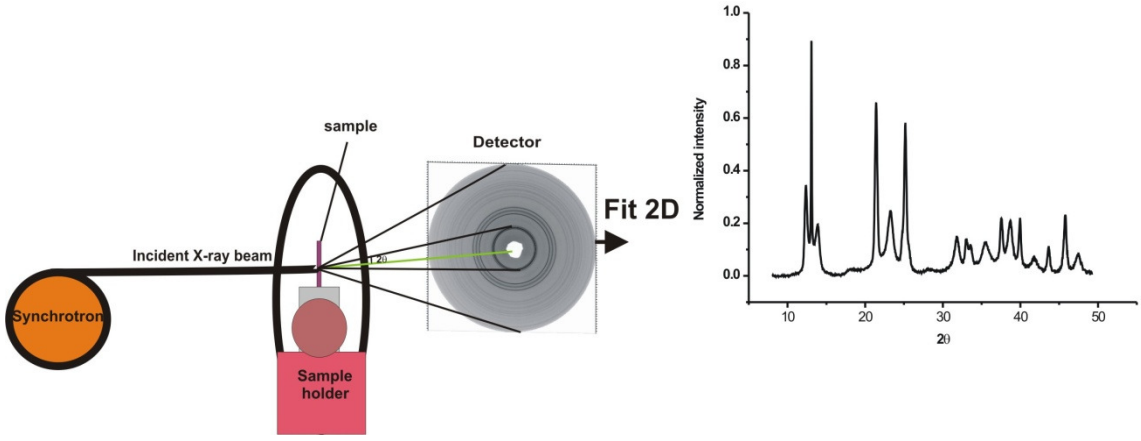

Figure 21 Left: General schematic diagram of powder diffraction. Right: radially averaged intensity as a function of scattering angle obtained by using Fit2D program.

Chapter 5

5. Manganese (Mn) doped CdSe nanowires

In recent years, it is known that doping process is controlled by kinetics rather than by thermodynamics. It is important to know how adsorption of the dopant on the surface of the nanomaterial and its trapping influences the growth process. The success of doping depends on the surface morphology, nanocrystal shape and surfactants in the growth solution. In case of Mn doped CdSe nanowires, both the Cd and Mn are divalent, the surfactant molecules can form bonds to Mn atoms as well as Cd surface atoms. Therefore, the doping of Mn in CdSe nanowires depends on the surface energy of either wurtzite or zincblende facets. It is previously known that the surface energy of (001) Wz has highest surface energy (-2.43eV) amongst other W reflections in CdSe nanocrystals. This indicates that Mn dopants are introduced into nanowires along the growth direction and the doping is anisotropic depending on the surface energy[12].

5.1 Diffraction pattern and the peak positions

The X-ray diffraction patterns(XRD)s of all samples as a function of θ are extracted from CCD images and plotted as a function of q as shown in figure 22. The diffraction pattern of both the doped and undoped sample provide an admixture of wurtzite and zinc-blende crystal structures. These patterns show dominantly W crystal structure rather than ZB. All the peaks in the diffraction patterns are indexed by the Miller indices of either Wz or ZB structure. There are no peaks related to alloy of Mn and other compounds. The positions of Bragg peaks of Wz and ZB structure are calculated using d spacing ($d=2\pi/q$) and structure factor[38]. Some selective peaks from fig.22 are zooming and show in figure 23 for more clarity and quantitative comparison.

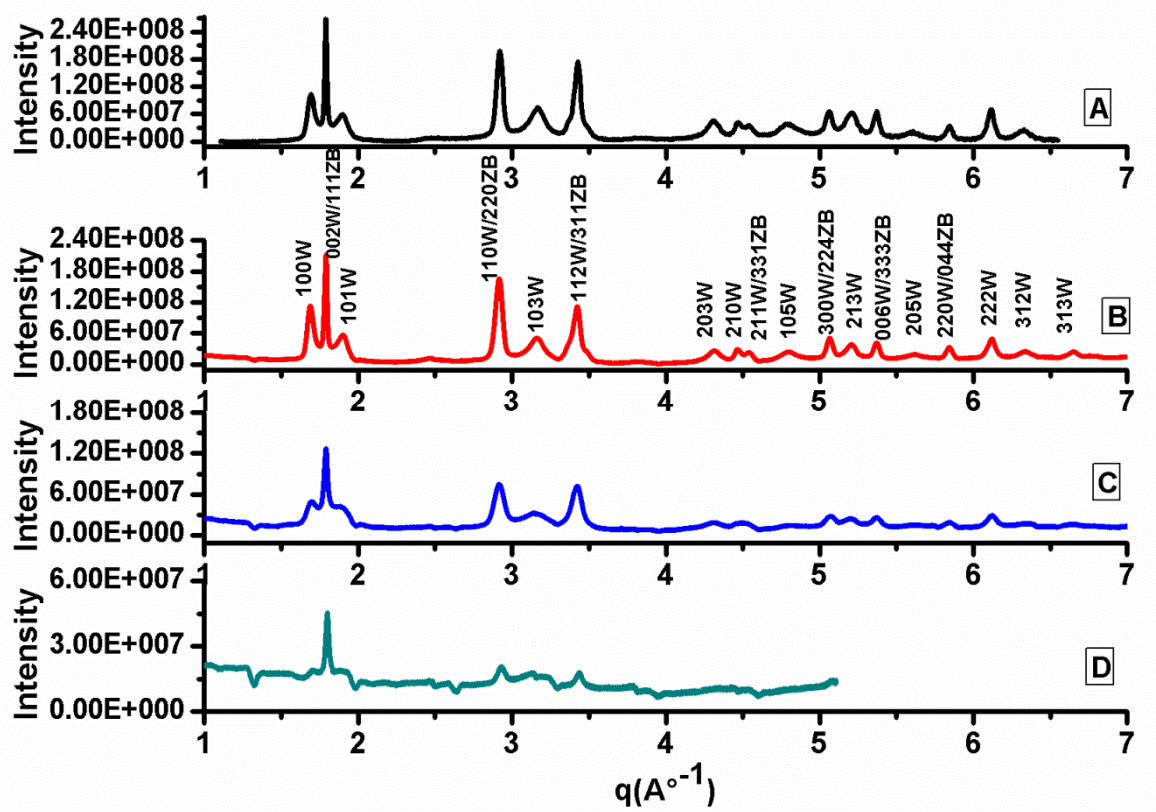

Figure 22 Diffraction pattern of A) undoped CdSe B) 0.25Mn-CdSe C)1.0Mn-CdSe and D) 2.0Mn-CdSe nanowires.

The black curve on the fig.(23) is the simulated powder diffraction curve from the model structure of CdSe NW. The model structure was created according to the undoped sample (red curve) parameters like as hexagonal lattice constant *a* and *c*, the *z*-position of Cd, radius of the NW along the *ab*-plane, height of the NW along c-axis and stacking fault parameters. The first three peaks, the normalized intensity of the simulated pattern is slightly different for the intensity of experimental peaks but the FWHM and the peak positions are same. The simulated and undoped peaks of 110W/220ZB and 103W are comparable but the 112W/331ZB simulated peak is highly broadened and low in intensity as comparing with the experimental one. The XRD pattern clearly shows that the reflection along the 002W direction is the dominant one and its intensity is much higher than the other reflections in simulated and experimental curves. The peak broadening on 103W and 112W/331ZB are highly influenced by the stacking fault parameters. It is observed that the intensity of reflections decreases as the doping concentration of Mn within CdSe NWs increases.

According to kinematical diffraction theory, the intensity of the Bragg peaks is related to the square of the atomic form factor which in turn depends on the atomic positions within the unit cell and atomic number Z. When Mn atom is doped within a CdSe NWs, the smaller Mn^{2+}

Diffraction pattern and the peak positions

ions occupy substitution sites in the CdSe lattice replacing the Cd^{2+} ions which changes the atomic

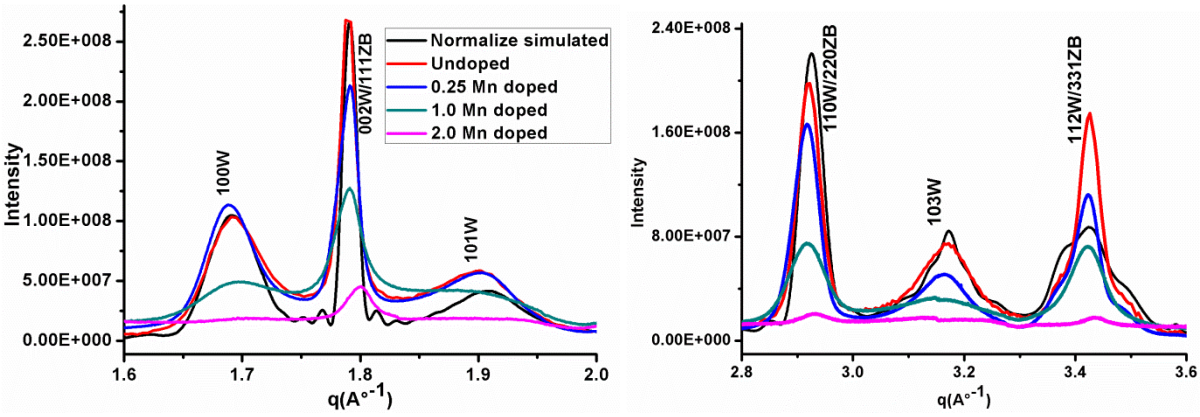

Figure 23 XRD pattern shows the intensity and peak broadening of the nanowires.

form factor thus changes the intensity of the peaks. It is clearly seen for the 2.0Mn-CdSe sample shown in figure (23), that the pure Wz peaks are highly broadened and no peaks we observed for q value higher than 5 A^{o-1}. This is explained by the high disorder in the crystal lattice. Additionally, the reflections from highly doped sample as slightly shifted towards higher q values indicating the lattice contraction in the NWs as expected due to smaller Mn radius.

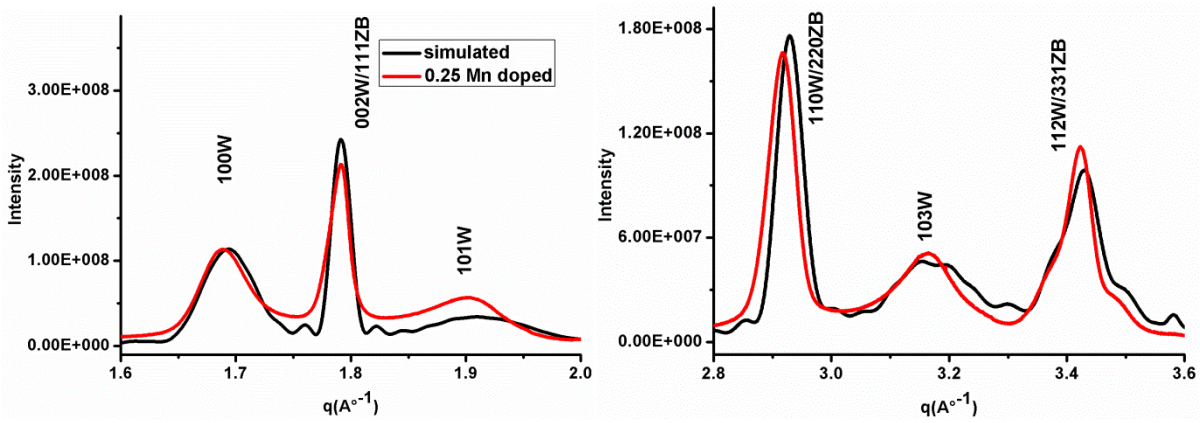

Figure 24 Comparison between the simulated (black curve) and experimental (red curve) diffraction pattern of 0.25Mn doped CdSe nanowires.

For the 0.25Mn doped sample the normalized simulated and experimental peaks are fitted better than undoped sample the fit is almost perfect except for 101W peak. The different parameters used for the simulation of 0.25Mn doped sample demonstrate the influence of Mn^{+2} ions on the structure of CdSe NWs. From fig. 24 the damping of intensity in X-ray diffraction pattern and highly peak broadening effect on 103W and 112W/331ZB can be understood by inclusion of dopants which create different stacking faults (growth fault and

deformation fault) in NWs. The twinning of lattice boundary (ZB to Wz and vice-versa) is due to the fast NW growth and small energy difference between W and ZB structures[12].

The anisotropic intensity variation between experimental and simulated pattern can be explained by texture like structure of powder NWs. Because of the very thin and long NWs they can form bundles of many NWs which may effects the intensity of certain reflections.

For the doped samples the bigger Cd^{2+} ions are replaced by slightly smaller Mn^{+2} ions as compared to the undoped sample however, no lattice contraction in 0.25Mn-CdSe and 1.0Mn-CdSe samples is observed except in case of highly doped (2.0Mn-CdSe) sample. The peak shift towards the higher q value reduces the lattice constant caused by the replacement of Cd atoms with small Mn atoms[39, 40]. The lattice constant ***a*** is calculated using equation 2.6.3 from in- plane reflections and the lattice constant **c** is calculated from out of plane reflections. The scenarios of lattice parameters are given in table 3.

Table. 3 Lattice parameters of undoped and Mn-doped CdSe nanowires.

	Lattice parameters	
	a(A°)	**c(A°)**
Theoretical	4.299	7.010
Undoped CdSe	4.2936±0.009	7.0175±0.0083
0.25Mn-CdSe	4.2936±0.009	7.0175±0.0083
1.0Mn-CdSe	4.2936±0.009	7.0175±0.0083
2.0Mn-CdSe	4.27366±0.00376	6.97996±0.00234

Error in lattice parameter can be calculated as a function of the angle of diffraction

$$d = \frac{\lambda}{2sin\theta} \Rightarrow \frac{d(d)}{d\theta} = \frac{-\lambda cos\theta}{sin^2\theta}$$

$$(Error\ in\ lattice\ parameter)\frac{d(d)}{d} = \frac{-d\theta}{tan\theta} = \frac{\Delta a}{a}$$

This relation shows that those peaks which we taken from the higher diffraction angles provide a smaller error in calculation of lattice parameters.

5.2 Dopant influences on intensity variation.

In diffraction pattern, it is observed that of the some of the ZB peaks coincide with the W peaks for all samples. First we that consider the NW consist of small portion of ZB structure units and nearly perfect Wz structure without any random stacking faults. Then the content of ZB structure x can be calculated using the intensity ratio between pure Wz and mixed Wz/ZB structure peaks. For example, the intensity of a mixed Wz/ZB (111ZB/002W) and a pure W (100W) reflection can be expressed as[8]:

$$F_{ex}^2(^{111ZB}/_{002W}) = xF_{cal}^2(111ZB) + (1-x)F_{cal}^2(002W) \qquad (5.2.1)$$

$$F_{ex}^2(100W) = (1-x)F_{cal}^2(100W) \qquad (5.2.2)$$

Here, F_{ex}^2 is the measured and F_{cal}^2 is the calculated structure factor of the pure W and ZB structure. The intensity ratio of pure W to mixed W/ZB reflections is shown in table 4.

Table. 4 Intensity ratios of pure W to W/ZB reflections and ratios of out-of –plane to in-plane reflections.

Sample	$\frac{\mathbf{100W}}{\mathbf{002W/111ZB}}$	$\frac{\mathbf{002W/111ZB}}{\mathbf{110W/220ZB}}$
CdSe	**1.06**	**0.42**
0.25Mn-CdSe	**1.02**	**0.44**
1Mn-CdSe	**0.52**	**0.51**
2Mn-CdSe	**0.20**	**1.64**

The change of the intensity ratio of pure Wz (100W) to Wz/ZB (002W/111ZB) reflections of different samples shows that the Wz content decreases for increasing the Mn concentration. The decrease of the intensity ratio of pure W to W/ZB reflections indicates the phase composition in the NWs. This is because of the different amount of structure factors for Wz and ZB reflections. The calculated value of F_{111ZB}^2 is 42651 for cubic closed packed system inclusion of the multiplicity factor, it is greater than the F_{002W}^2=20665 for hexagonal closed packed system. Therefore, the decrease in intensity ratio Wz/ZB indicates that the NWs growing process is in favor of ZB phase under Mn influence. The doping is preferentially occurred along highly reactive (001) facets rather than less reactive (110) facets[12, 41] that means the ZB structure is more pronounced along the 002W/111ZB peak than 110W/220ZB

peak and the intensity ratio of these peaks are increases by increasing the doping. More specifically, the ratios of structure factors of Mn doped and undoped samples are shown in Fig. 25.

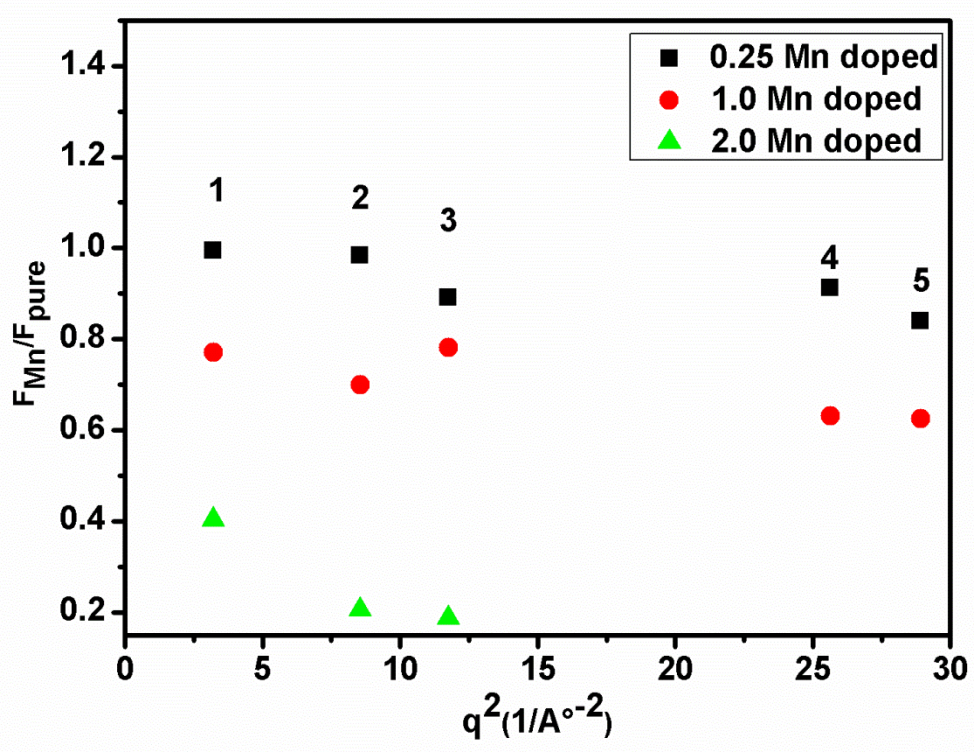

Figure 25 The ratio of structure factor of experimental Mn doped and undoped sample.

For experimental calculation of structure factor the intensity was taken as area under the curve from Gaussian fit and used equation 2.6.4 by considering the LP factor, Multiplicity factor and static Debye Waller factor (DWF). The value of these factors for the calculation of $\mathbf{F_{Mn}/F_{pure}}$ is summarized in table 5.

Table. 5 Structural parameters for the calculation of structure factor.

Peak position no.	LP factor	M factor	Static DWF
1	397.38	2	0.97771
2	147.85	6	0.94192
3	106.75	12	0.92104
4	47.08	6	0.8348
5	41.60	6	0.81638

For constant temperature there is no difference between thermal and static DWF. The decrease in the ratio of structure factor reveals the decrease in the intensity of doped sample.

In 2.0Mn-doped sample the damping occurred very fast therefore we did not get the intensity for higher q value. The ratios of structure factors for all reflections are not constant which demonstrate the anisotropic properties in the NWs created due to doping.

5.3 Effect of stacking faults on CdSe nanowires.

As described in chapter 3, the stacking faults appearing in the NW are either in form of growth fault or deformation faults. These faults are occurred if either one layer is stacked at the wrong position during the growth or one layer is shifted parallel to another layer. In order to characterize the crystal structure of NWs it is important to emphasize the stacking fault (or polytypism). In CdSe, one layer is composed of pair Cd atom and one pair Se atom defining a double layer. A normal wurtzite sequence is ABABAB and ZB sequence is ABCABC. The stacking fault in WZ structure is regarded as a single segment of the ZB structure and vice-versa, which produces a change in the diffraction pattern[42]. The misplacement of double layer in WZ phase giving the sequence AB<u>AB</u>|<u>C</u>BCB with the fault line between B and C, automatically creates a single unit of ZB structure (<u>ABC</u>). The change of ZB to WZ sequence is AB<u>CBCA</u> shows the fault in between B and C double layer. These faults creates in the NWs produce the decrease the intensities and increases the FWHM of Bragg's reflection. Figure 24 demonstrates the deviation of FWHM due to stacking faults for different samples, undoped, 0.25 Mn doped, and 1.0 Mn doped.

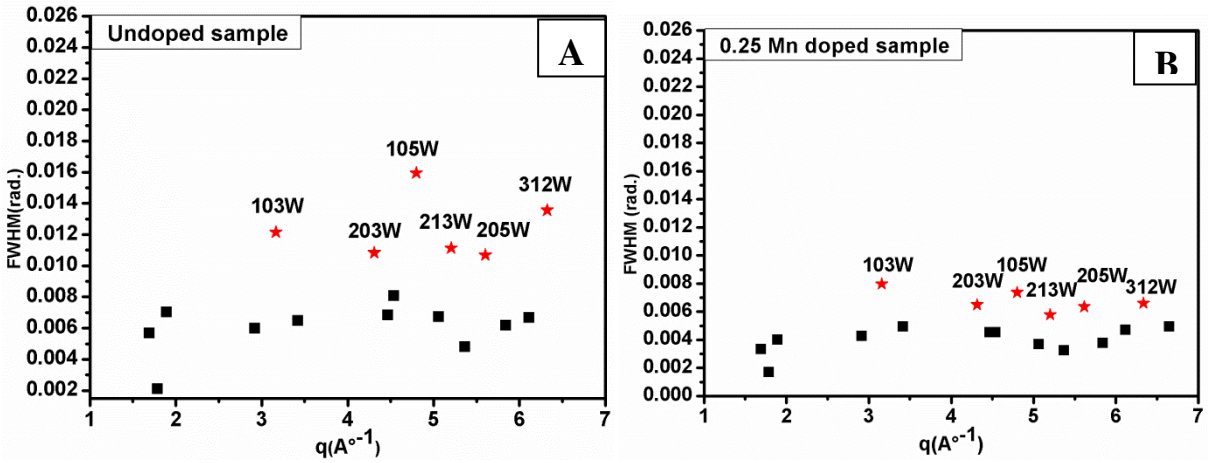

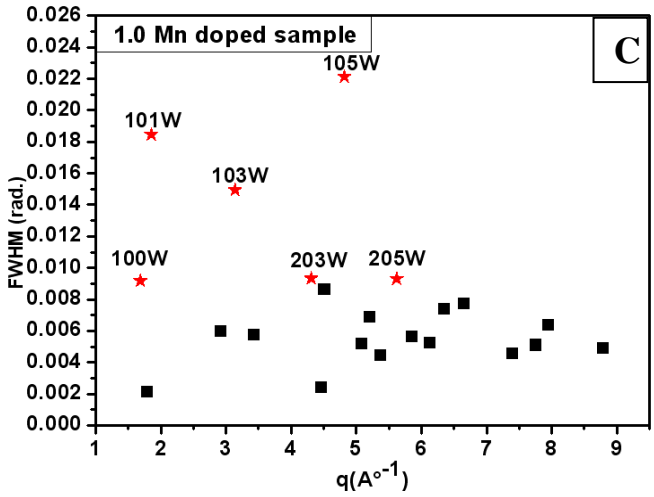

Figure 26 FWHM of diffraction peaks A) undoped CdSe NW B) 0.25Mn-CdSe NW C) 1.0Mn-CdSe NW with indication of certain reflection shows the influenced of stacking faults.

In the undoped sample, the deviation of FWHM from the average is seen in reflections like 103W, 203W, 105W, 205W, 213W, 312W. The same pattern occurred in doped samples but the deviation is low in 0.25 Mn doped sample and very high in 1.0 Mn doped sample. The dopants would react differently with the nanowire as a function of size[43]. The peaks with $h-k=3n$ are sharp because they are independent of stacking faults but the peaks with $h-k=3n\pm1$ are broadens due to the faults[8, 38]. This can be clearly seen for all samples. The peak broadening of some reflection which is influenced by the stacking faults are given in table 6.

Table. 6 FWHM of stacking faults reflections of undoped and Mn-doped samples.

Plane	Undoped	0.25Mn doped	1.0 Mn doped	2.0 Mn doped
Hkl	$\Delta_{2\theta}(^\circ)$	$\Delta_{2\theta}(^\circ)$	$\Delta_{2\theta}(^\circ)$	$\Delta_{2\theta}(^\circ)$
101W	0.40	0.23	1.06	2.44
103W	0.70	0.46	0.86	4.70
203W	0.62	0.37	0.53	
105W	0.91	0.42	1.27	
213W	0.64	0.33	0.40	
205W	0.61	0.36	0.53	

By neglecting the other broadening effects(diffuse scattering, strain) the measured full width at half maximum intensity is given by [8, 38].

Effect of stacking faults on CdSe nanowires

$$\Delta_{2\theta} = \left(\frac{360}{\pi^2}\right) tan\theta |l| \left(\frac{d_{hkl}}{c_w}\right)^2 (3\alpha + n\beta) \qquad (5.4.1)$$

Where, $n = \begin{cases} 3 & for\ l\ even \\ 1 & for\ l\ odd \end{cases}$, α and β are the probability of growth and deformation fault. Peak broadening in different samples shows the variation of stacking fault (SF) due to the effect of Mn atoms replacement of Cd atoms. Increase in the concentration of Mn atoms increases the number of SFs in CdSe NWs. The effect of deformation faults on intensity for peak with *l* odd and for peak with *l* even is different as seen in chapter 3.3. The peak broadening due to deformation fault is same for either *l* odd or even but for the growth fault broadening is different for *l* odd and even. Stacking faults (growth fault and deformation fault) doesn't affect the peak asymmetries and peak displacement in powder pattern. Using the measured FWHM intensity given in equation (5.4.1) we can roughly calculate the value of α and β. For this purpose, we choose the broadening peak 312W for *l* is even and other broadening peak for *l* is odd are 103W, 203W, 105W and 205W respectively. The value of α and β are found to be different for different peak positions. The average value of α and β by solving the equation (5.4.1) using above broadening peaks are summarized in table 7.

Table. 7 Experimental and simulated growth fault and deformation fault in CdSe nanowires.

Samples	**Growth fault (α)**		**Deformation fault (β)**	
	Experimental	simulated	Experimental	Simulated
Undoped CdSe	**0.025±0.004**	**0.05**	**0.40±0.03**	**0.15**
0.25 Mn doped	**0.04±0.015**	**0.09**	**0.30±0.024**	**0.12**
1.0 Mn doped	**0.18±0.05**		**0.19±0.04**	

For undoped CdSe NW the value of α is calculated 0.025±0.004 and β is 0.40±0.03 but for the 0.25 Mn doped CdSe NW sample the value of α increases and β decreases. The simulated value of α and β given in table 7 was used to simulate the undoped and 0.25Mn doped CdSe NW. Both Experimental and simulated result agrees with the influence of Mn dopants on CdSe NWs enhanced the growth fault and reduces the deformation fault. This result also demonstrates that the increase in Mn concentration on CdSe NWs favors the ZB phase structure.

5.4 Coherence length in CdSe nanowires

In growth mechanism, the NWs growth same phase until there is no any defects occurred in crystal. Here, the coherence length of NWs in a particular reflection is length of the same phase (either W or ZB) of that direction. The coherence length of such reflection can be calculated using well-known Scherrer equation[8, 38].

$$coherence\ Length\ (L) = K\lambda/\Delta_{2\theta}cos\theta \qquad (5.5.1)$$

where θ is the Bragg angle, K is constant and $\Delta_{2\theta}$ is the FWHM of Bragg reflection.

Table. 8 Coherence length (nm) of undoped and Mn-doped CdSe nanowires.

plane	CdSe	0.25Mn-CdSe	1.0Mn-CdSe	2.0Mn-CdSe
002W/111ZB	35.97	27.8	21.3	22.5
110W/220ZB	12.76	11.1	7.8	8.3
300W/224ZB	11.82	13.0	9.1	
006W/333ZB	16.65	14.8	10.7	
220W/044ZB	13.09	12.7	8.5	
100W	13.29	14.1	5.1	5.4

The coherence length of NWs along the growth axis, 002W/112ZB for undoped sample is found around 36nm and decreases to 21nm for 1.0 Mn doped sample. The coherence length along 110W/220ZB direction gives the diameter of the NWs which is the good agreement of the NWs diameters found in TEM images. The doping on the NWs enhances the anisotropic SF properties and affects the intensity and peak broadening. The peak broadening decreases the coherence length as increase the doping concentration till 1.0 Mn doped sample. In 2.0 Mn doped sample, the coherence length of NWs is increases due the highly distorted crystal structure. There was some discrepancy of coherence length along growth direction 002W and 006W in all samples. This discrepancy may be defined as the overlapping of 302W peak on 006W peak because the q-space for these peaks is 5.37026$A^{\circ-1}$ and 5.37623$A^{\circ-1}$ respectively.

5.5 Strain analysis on Mn doped CdSe nanowires

Strain is the physical properties that describes the structural deviation of the crystal from the ideal bulk state[44]. The Williamson Hall method[45] is used to isolate the contribution of strain and particle size in the peak broadening in XRD pattern. In order to obtain more

quantitative information about size and strain of NWs the XRD pattern of CdSe NWs was convoluted with Gaussian function and the peak broadening can be expressed as[46, 47]:

$$\Delta_{2\theta} = \frac{k\lambda}{D\cos\theta} + \varepsilon \tan\theta \qquad (5.3.1)$$

where $\Delta_{2\theta}$ is the peak broadening, $k \approx 1$, λ is the wavelength, ε is the strain. Besides crystallite size and strain broadening there is also instrumental broadening in diffraction pattern which we have done the flat-field correction and background subtraction.

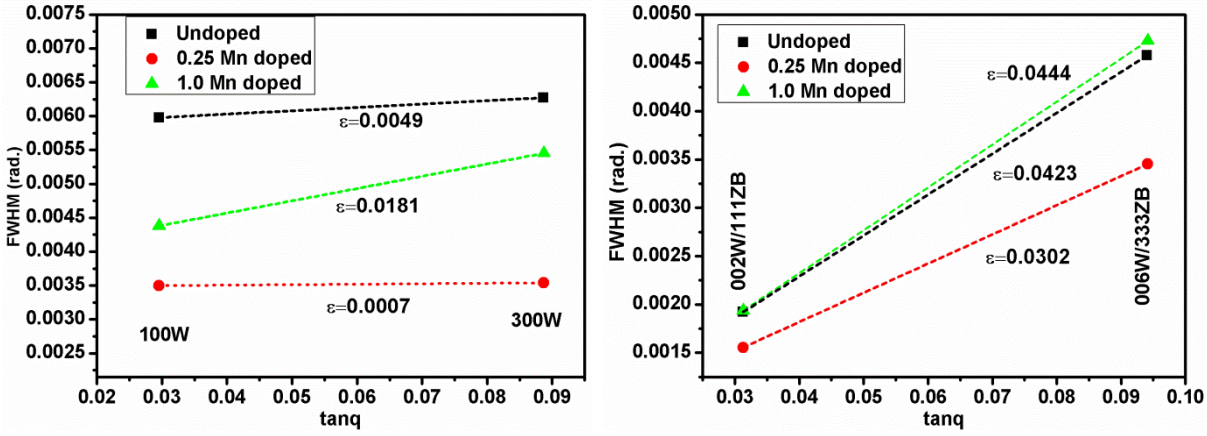

Figure 27 Strain analyses along the growth direction 00l(right) and the h00 direction (left).

Using relation (5.3.1) the strain along growth direction and h00 direction could be obtained from the slope of the fitting curves in fig. 27, while the intercept gives the size broadening. The strain along the both direction decreases for small doping (0.25 Mn doped) and increases for high doping (1.0 Mn doped). The decrease in strain in 0.25Mn doped sample may be strain relaxation due to small doping on the surface of NW caused by the ratio of surface to bulk atoms grows[48]. In both cases the fitting curves do not pass through the origin reveals that the strain is size dependent and this size dependent strain increases as NW diameter decreases. The doping of Mn^{2+} ions within the CdSe NWs is anisotropic such that the dopants are considered to bind the most reactive facets. Thus, the doping will preferentially affect the most reactive (001) facets rather than less reactive (110) facets[12, 41]. The strain along the growth direction is high which is because of the most reactive facets create more defects as compared to the other direction.

6. Cobalt (Co) and Iron (Fe) doped CdSe nanowires

In this chapter, we report on CdSe NW doped with different concentration of Co and Fe. They are characterized by X-ray diffraction measurement at PETRA III beamline P08 using a point detector with wavelength of 0.66A°. Motivated by different types diluted magnetic semiconductors, Co^{2+} and Fe^{2+} doped II-VI nanowires can be performed in nanoscale device application because of their shape and size are controlled in a strong quantization regime by wet chemical method[40, 49, 50].

6.1 Diffraction pattern of Co and Fe doped CdSe nanowires.

In figure 28 and figure 29 the XRD pattern of Co and Fe doped CdSe nanowires are shown respectively. XRD pattern of both Co and Fe doped samples shows the admixture of W and ZB structure as seen in undoped and Mn doped samples. It was observed that many sharp peaks appeared which are not come from the CdSe NWs as indicated by downward green arrow line in both pattern. These peaks have very low point resolution therefore it may not come from the sample but from experimental equipment. The peaks causing from CdSe NWs in the diffraction patterns are indexed by the Miller indices like as done for Mn doped samples. Omitting the artifact peaks in diffraction pattern it can be seen in Co doped sample the intensity of the peaks drop down (except for 002W peak) accordingly increases the Co concentration. In case of Fe doped samples the intensity increases from 0.25 to 0.5 and then decreases to 1.0 Fe doped sample. The 101W and 112W/311ZB peaks of 0.25 Co and Fe doped samples are unexpectedly sharp which cannot be seen in previous samples and also in simulated pattern. The sharpness of these peaks may be due to the overlapping of artifact peaks because there are many artifact peaks are clearly seen in diffraction pattern.

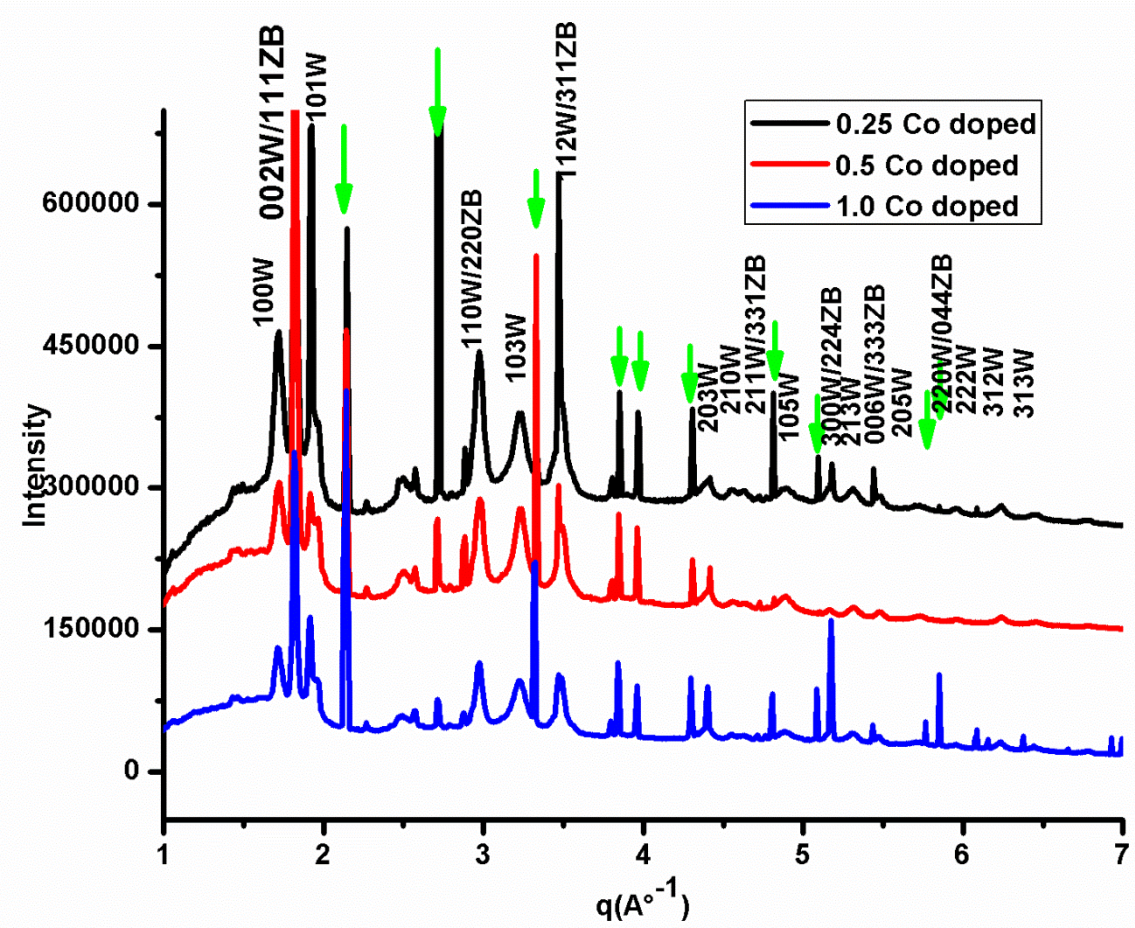

Figure 28 XRD pattern from different concentration of Co doped CdSe nanowires.

When Co or Fe doped within a CdSe NWs the smaller ions of these dopant occupy substitution sites in the CdSe lattice by replacing the Cd^{2+} ions. The replacement of these ions produces the intensity variation effects as well as other defects in the crystal structure. However, the replacement of small Co^{2+} or Fe^{2+} ions does not change the q space in all samples i.e. there is no lattice contraction in NWs structure due to doping.

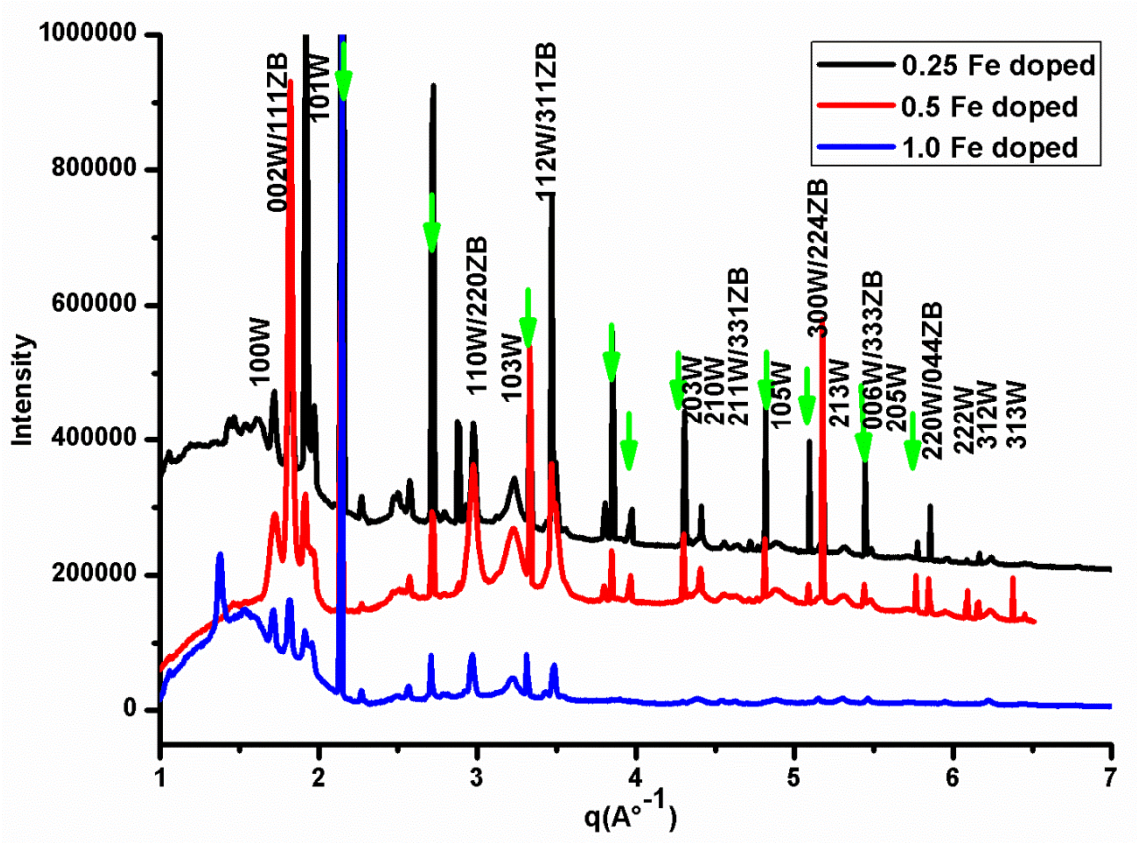

Figure 29 XRD pattern from different concentration of Fe doped CdSe nanowires.

In doped samples, either Co^{2+} or Fe^{2+} ions replaced to the slightly larger Cd^{2+} ions in comparison to the undoped sample. The in-plane lattice parameter **a** and out-of-plane lattice parameter **c** can be calculated using equation in equation 2.6.3 with corresponding reflections. The lattice parameters of the Co doped and Fe doped samples are present in table 9. The errors in the lattice parameter are calculated like as done for the Mn doped samples. We observed that there is no change in lattice parameter for all concentration of Co and Fe doped samples within experimental uncertainties.

Table. 9 Lattice parameter of cobalt and iron doped cadmium selenide nanowires.

	Lattice parameters	
	a(A°)	**c(A°)**
Theoretical	4.299	7.010
Undoped CdSe	4.2936±0.009	7.0175±0.0083
0.25Co-CdSe	4.27015±0.0383	6.97598±0.0486
0.5Co-CdSe	4.27015±0.0383	6.97598±0.0486
1.0Co-CdSe	4.27015±0.0383	6.97598±0.0486

0.25Fe-CdSe	4.27992±0.0255	6.96904±0.0496
0.5Fe-CdSe	4.27992±0.0255	6.96904±0.0496
1.0Fe-CdSe	4.27992±0.0255	6.96904±0.0496

6.2 Effects of intensity due to dopants (Co and Fe) on CdSe nanowires.

The intensity ratio of pure W to W/ZB ratio determines the phase change in NW created by stacking faults. The decrease in such a ratio indicates the increase in ZB structure of CdSe NW because the structure factor and the corresponding multiplicity factor of ZB peak is higher than the W peak. The intensity ratios of 100W to 002W/111ZB decreases from 1.06 to 0.23 for undoped to 0.50Co-doped NW and then slightly increase for 1.0Co-doped sample. In case of Fe-doped samples the intensities ratios is decreased than the undoped sample but the decreasing order is not follow the order of increasing Fe concentration. The decreasing intensity ratio of pure W to W/ZB peak indicate that the Co^{2+} and Fe^{2+} ions in CdSe NW enhance the ZB structure.

Table. 10 Intensity ratios of pure W to W/ZB reflections and ratios of out-of –plane to in-plane reflections.

	Intensity ratio of Undoped sample	**Intensity ratio of Co doped samples**			**Intensity ratio of Fe doped samples**		
Peak		0.25Co-CdSe	0.50Co-CdSe	1.0Co-CdSe	0.25Fe-CdSe	0.5Fe-CdSe	1.0Fe-CdSe
$\frac{\mathbf{100W}}{\mathbf{002W/111ZB}}$	1.06	0.70	0.23	0.33	0.20	0.18	0.64
$\frac{\mathbf{002W/111ZB}}{\mathbf{110W/220ZB}}$	0.42	1.39	3.23	2.37	3.49	0.25	1.48

The intensities ratios of 002W/111ZB to 110W/220ZB peak increases for both Co and Fe doped samples as compared to undoped sample. The SFs effect in 110W peak is very low than 002W peak because of low surface energy. Thus the increment of out-of-plane and in-plane intensities ratios reveals the orientation of NW is more pronounced along the growth direction than radial direction due to doping. Fig.30 demonstrates the ratio of structure factor of doped and undoped samples. Structure factor ratio of Co doped and undoped sample decreases as increases the Co concentration which means the damping of intensity is dopant

dependent. For the Fe doped sample the structure factor ratio is highest in 0.50Fe doped NWs that may be due to the high volume of NW samples used in the experimental measurement.

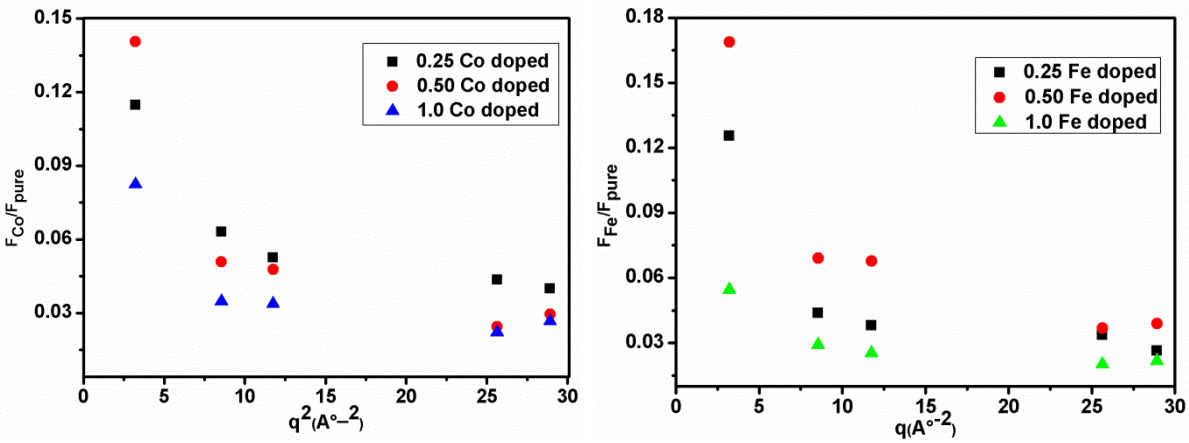

Figure 30 Left:- Ratio of structure factor of Co doped and undoped CdSe nanowires. Right:- Ratio of structure factor of Fe doped and undoped CdSe nanowires.

6.3 Efeect of stacking faults on Co and Fe doped CdSe nanowires.

The stacking faults effects on the CdSe Nws are demonstrated by the FWHM vs. q-space. The deviation of FWHM from the average is due to the SFs on the NWs. For different reflections the effect of SFs are different which is described in previous chapter. Increase in SFs on the NWs increases the FWHM in the diffraction pattern.

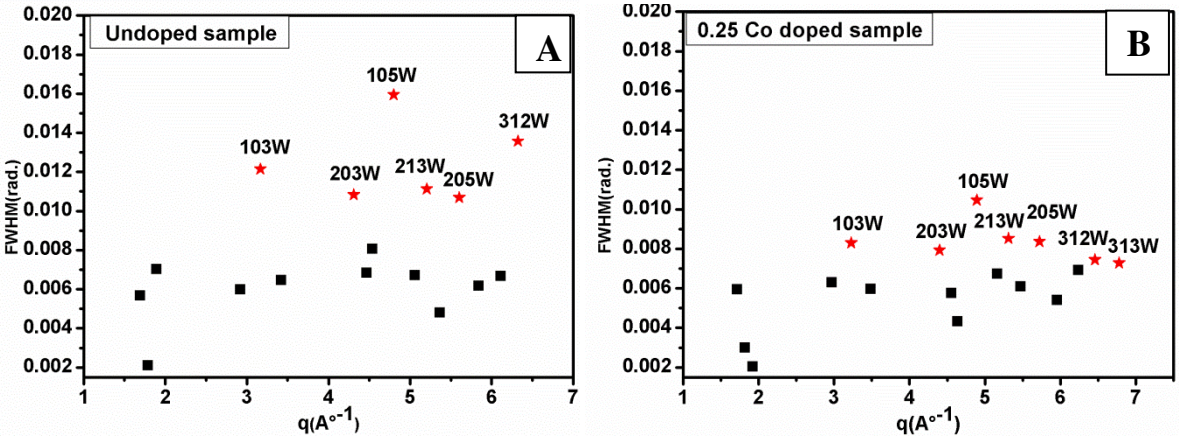

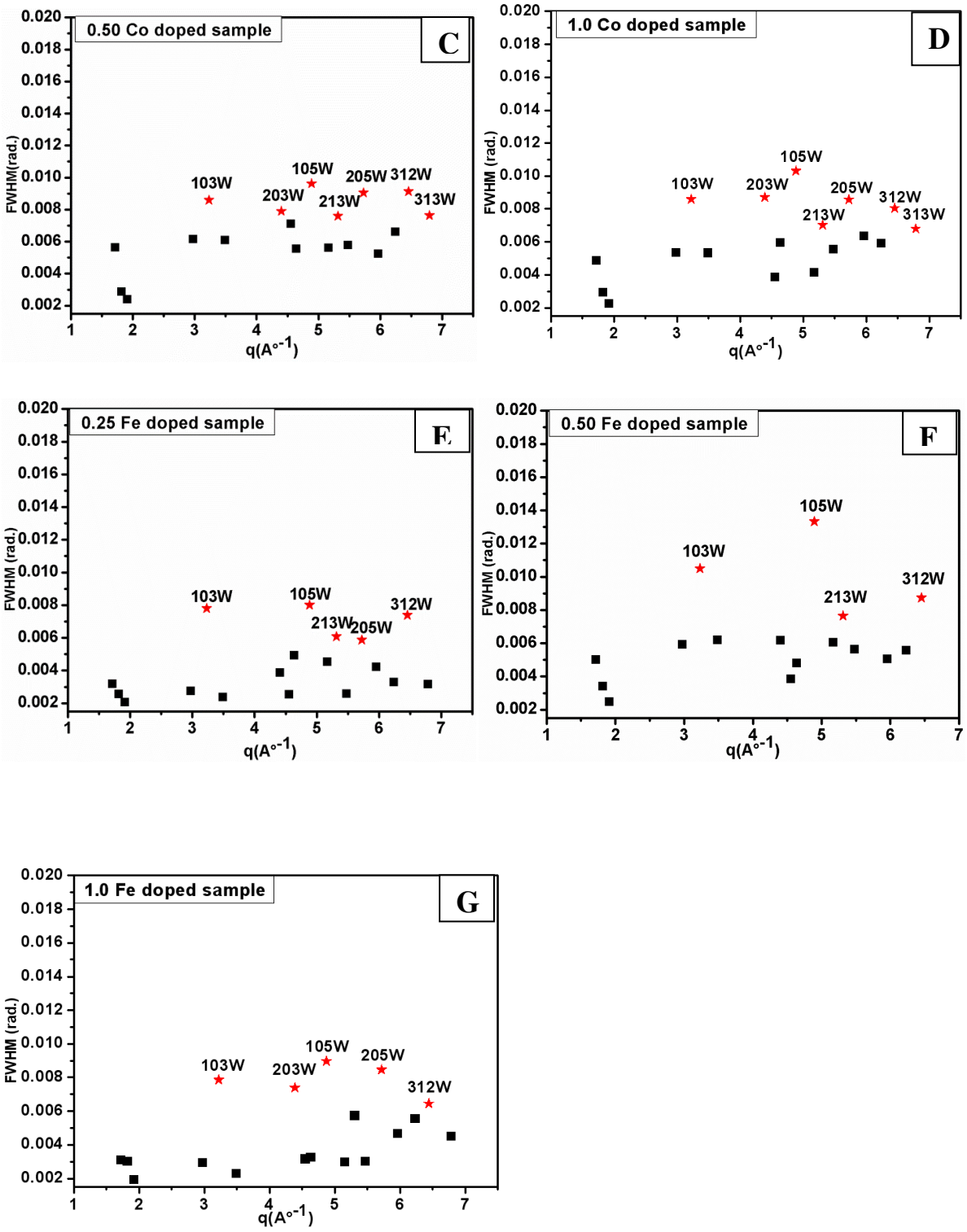

Figure 31 FWHM of diffraction peaks of A) undoped CdSe B) 0.25Co- CdSe C) 0.50Co-CdSe D) 1.0Co-CdSe E) 0.25Fe- CdSe F) 0.50Fe-CdSe G) 1.0Fe-CdSe Nws with indication of certain reflection shows the influenced of stacking faults.

As like in undoped CdSe NWs, the Co and Fe doped samples also shows the SFs effects in same reflections as: 103W, 203W, 105W, 205W, 213W, 312W indicated by red star symbol. For Co doped samples, the peak broadening effects due to stacking faults are seen decreasing

which is because of the decrease in deformation faults in the doped samples. The SF effect for all Co doped samples looks similar and not influenced according to increasing the Co concentration. In 0.25 Fe doped CdSe NWs sample the FWHM of many peaks shows increasing of peak sharpness as compared to Co doped sample. The stacking fault effect is highly dominant for the peak 103W and 105W in 0.50 Fe doped sample and decrease the peak sharpness as compared to the 0.25 Fe doped sample.

6.4 Coherence length of Co and Fe doped CdSe nanowires.

To get the quantitative information about the coherence length (size), the XRD pattern of Co and Fe doped CdSe nanowires are convoluted with Gaussian function and FWHM is expressed like as equation 5.5.1. The coherence length obtained along the growth direction for Co doped samples are 21nm and for the Fe doped samples the coherence length decreases from 24 to 21 nm from 0.25Fe doped sample to 1.0Fe doped sample. The diameter of the NWs along the ab-plane found for the Co doped samples changes from 10-12nm and for the Fe doped samples are changes from 23-21nm.

Chapter 6

6. Discussion and Outlook

In this work diluted magnetic CdSe NWs were synthesized successfully by SLS method. For the preparation of such NWs the doping process is confined within the Bi nanocatalysts. Fast and non-destructive X-ray powder diffraction technique is used to estimate the structural parameters. The model structures of CdSe NWs are simulated using DISCUS program and calculated the powder diffraction pattern by the application of Debye formula. In case of Mn doped NW, the dopant influence can be clearly observed in XRD pattern and via calculations. However, the doping effect is ambiguous for Co and Fe doped NWs. A detailed analysis of the structural properties shows that all doped NWs exhibit a combination of Wz and ZB crystal structures like as undoped sample. Decrease in intensity ratio of pure Wz to W/ZB peak shows change in phase composition of Wz to ZB in all doped samples. It is observed that in highly Mn doped sample (2.0 Mn doped) the effect of Mn concentration causes highly broadened in Wz peak, lattice contraction and lattice distortion in the NWs. The strain and crystallite size (coherence length) is also dopant dependent and are extracted from Williamson Hall relation. The coherence length along the growth direction found to be 36nm to 21nm from 0-1.0 Mn doped sample. The diameter of the NWs from the XRD measurements are found to be 14nm to 9nmfrom 0-1.0 Mn doped sample which is the good agreement with the TEM measurements. The SFs on the NWs are observed in FWHM vs. q space pattern. SFs effects are observed those peaks with $h - k = 3n \pm 1$. Two types of SFs such as growth fault and deformation fault are calculated using the peak broadening in the diffraction pattern. The average growth fault increases from 0.025 to 0.16 and the average deformation fault decreases from 0.36 to 0.21 as increases the doping concentration from 0-1.0 Mn doped samples. The increase and decrease of SF parameters created by Mn^{2+} ions in CdSe NWs agrees with the model structure of simulated CdSe NWs.

Historically, the doping of Mn^{2+} ions in to a CdSe nanostructure is problematic because of the intrinsic self purification[51] and reduced surface adsorption of dopants[41]. In 2007, Sung et.al[52] synthesized the Mn-doped CdSe nanocrystal using micelle technique. The nanocrystal has the ZB structure and dopant influence produces the lattice contraction and

increase the crystallnity of NWs. In 2010, first time Mn doped CdSe NWs were synthesized successfully using SLS method[12]. They reported the effect of Mn^{2+} ions on CdSe NWs produce lattice contraction and the dopants are preferentially adsorbed along the growth direction which agrees with our result. Recently, Zhen Li et.al[40] reported Co^{2+} CdSe NW prepared by SLS method they found increase in Co concentration leads to a peak shift of reflection peaks to higher angles in their XRD pattern, which cannot be clearly observed in our diffraction pattern.

The success of doping Mn^{2+} ions into CdSe NWs opens the road for the application of nanoscale devices. The variation of all structural parameters created by dopants is not well understood. Therefore, it is required to improve the synthetic control over dopant incorporation and tuning of structural parameters of the NWs. For the future work, the experiment has to be done more precisely and the volume of powder NW from which the X-rays are diffracted, taken into consideration for the normalization of intensity. The improvements of model structure are required to study other structural defects like as strain, point defect, vacancies along with the SFs.

List of Figures

List of figures

List of Tables

Bibliography

1. Klimov, V., et al., *Optical gain and stimulated emission in nanocrystal quantum dots.* Science, 2000. **290**(5490): p. 314.
2. Dahan, M., et al., *Time-gated biological imaging by use of colloidal quantum dots.* Optics Letters, 2001. **26**(11): p. 825-827.
3. Hu, X., G. Li, and J.C. Yu, *Design, fabrication, and modification of nanostructured semiconductor materials for environmental and energy applications.* Langmuir, 2009. **26**(5): p. 3031-3039.
4. Chen, C.C., et al., *Superparamagnetism Found in Diluted Magnetic Semiconductor Nanowires: Mn-Doped CdSe.* The Journal of Physical Chemistry C, 2008. **112**(46): p. 17964-17968.
5. Wolf, S., et al., *Spintronics: A spin-based electronics vision for the future.* Science, 2001. **294**(5546): p. 1488.
6. Beaulac, R., P.I. Archer, and D.R. Gamelin, *Luminescence in colloidal Mn2+-doped semiconductor nanocrystals.* Journal of Solid State Chemistry, 2008. **181**(7): p. 1582-1589.
7. Archer, P.I., S.A. Santangelo, and D.R. Gamelin, *Direct observation of sp-d exchange interactions in colloidal Mn2+-and Co2+-doped CdSe quantum dots.* Nano letters, 2007. **7**(4): p. 1037-1043.
8. Kurtuluş, Ö., et al., *X-ray investigation of CdSe nanowires.* physica status solidi (a), 2009. **206**(8): p. 1752-1756.
9. Li, Z., et al., *Controlled Synthesis of CdSe Nanowires by Solution–Liquid–Solid Method.* Advanced Functional Materials, 2009. **19**(22): p. 3650-3661.
10. Norris, D.J., A.L. Efros, and S.C. Erwin, *Doped nanocrystals.* Science, 2008. **319**(5871): p. 1776.
11. He, Z., et al., *Tuning electrical and photoelectrical properties of CdSe nanowires via indium doping.* Small, 2009. **5**(3): p. 345-350.
12. Li, Z., et al., *Diluted Magnetic Semiconductor Nanowires Prepared by the Solution–Liquid–Solid Method.* Angewandte Chemie International Edition, 2010. **49**(15): p. 2777-2781.
13. Proffen, T. and R. Neder, *DISCUS: a program for diffuse scattering and defect-structure simulation.* Journal of applied crystallography, 1997. **30**(2): p. 171-175.
14. Beaulac, R., et al., *Spin-polarizable excitonic luminescence in colloidal Mn2+-doped CdSe quantum dots.* Nano letters, 2008. **8**(4): p. 1197-1201.
15. Yu, J.H., et al., *Giant Zeeman splitting in nucleation-controlled doped CdSe: Mn2+ quantum nanoribbons.* Nature materials, 2009. **9**(1): p. 47-53.
16. Pietsch, U., V. Holý, and T. Baumbach, *High-resolution X-ray scattering from thin films to lateral nanostructures*. 2004: Springer Verlag.
17. Als-Nielsen, J., *Elements of modern X-ray physics*. 2011: Wiley.
18. Ibach, H., *Solid-state physics: an introduction to principles of materials science*. 2009: Springer Verlag.
19. Kittel, C. and P. McEuen, *Introduction to solid state physics*. Vol. 7. 1976: Wiley New York.
20. Crystallography, I.U.o., *International tables for X-ray crystallography*. Vol. 3. 1962: Kynock Press.
21. Pecharsky, V.K. and P.Y. Zavalij, *Fundamentals of powder diffraction and structural characterization of materials*. Vol. 69. 2009: Springer Verlag.
22. He, B.B., J.H. Reibenspies, and N. Bhuvanesh, *Two-Dimensional X-Ray Diffraction.* Powder Diffraction, 2010. **25**: p. 200.
23. Niederdraenk, F., et al., *Structure of small II-VI semiconductor nanoparticles: A new approach based on powder diffraction.* physica status solidi (c), 2007. **4**(9): p. 3234-3243.
24. Neder, R.B. and T. Proffen, *Diffuse scattering and defect structure simulations: a cook book using the program DISCUS*. 2008: Oxford University Press, USA.
25. Fadda, A. and G. Fadda, *An evolutionary algorithm for the prediction of crystal structures.* Physical Review B, 2010. **82**(10): p. 104105.

26. Price, K.V., R.M. Storn, and J.A. Lampinen, *Differential evolution: a practical approach to global optimization*. 2005: Springer Verlag.
27. Welberry, T.R., *Diffuse x-ray scattering and models of disorder*. Vol. 16. 2004: Oxford University Press, USA.
28. Neder, R., et al., *Structural characterization of II-VI semiconductor nanoparticles.* physica status solidi (c), 2007. **4**(9): p. 3221-3233.
29. Grover, R.F. and D.R. McKenzie, *An efficient ab initio calculation of powder diffraction intensity using Debye's equation.* Acta Crystallographica Section A: Foundations of Crystallography, 2001. **57**(6): p. 739-740.
30. Wood, W. and F. Parker, *Monte Carlo Equation of State of Molecules Interacting with the Lennard-Jones Potential. I. A Supercritical Isotherm at about Twice the Critical Temperature.* The Journal of Chemical Physics, 1957. **27**: p. 720.
31. Rabani, E., *An interatomic pair potential for cadmium selenide.* The Journal of Chemical Physics, 2002. **116**: p. 258.
32. Binder, K. and A. Baumgärtner, *The Monte Carlo method in condensed matter physics*. Vol. 71. 1992: Springer-Verlag Berlin.
33. Wang, F., et al., *Solution-liquid-solid growth of semiconductor nanowires.* Inorganic chemistry, 2006. **45**(19): p. 7511-7521.
34. Wooten, A.J., et al., *Solution− Liquid− Solid Growth of Ternary Cu− In− Se Semiconductor Nanowires from Multiple-and Single-Source Precursors.* Journal of the American Chemical Society, 2009. **131**(44): p. 16177-16188.
35. Kuno, M., *An overview of solution-based semiconductor nanowires: synthesis and optical studies.* Phys. Chem. Chem. Phys., 2007. **10**(5): p. 620-639.
36. Kar, S., S. Santra, and H. Heinrich, *Fabrication of high aspect ratio core-shell CdS-Mn/ZnS nanowires by a two step solvothermal process.* The Journal of Physical Chemistry C, 2008. **112**(11): p. 4036-4041.
37. Hammersley, A., *FIT2D: an introduction and overview.* European Synchrotron Radiation Facility Internal Report ESRF97HA02T, 1997.
38. Warren, B.E., *X-ray Diffraction*. Chapt.3.3. 1990: Dover Pubns.
39. Karar, N., F. Singh, and B. Mehta, *Structure and photoluminescence studies on ZnS: Mn nanoparticles.* Journal of applied physics, 2004. **95**: p. 656.
40. Li, Z., et al., *Cobalt-doped cadmium selenide colloidal nanowires.* Chemical Communications, 2011.
41. Erwin, S.C., et al., *Doping semiconductor nanocrystals.* Nature, 2005. **436**(7047): p. 91-94.
42. Caroff, P., et al., *Controlled polytypic and twin-plane superlattices in III–V nanowires.* Nature nanotechnology, 2008. **4**(1): p. 50-55.
43. Xie, P., et al., *Diameter-dependent dopant location in silicon and germanium nanowires.* Proceedings of the National Academy of Sciences, 2009. **106**(36): p. 15254-15258.
44. Robinson, I. and R. Harder, *Coherent X-ray diffraction imaging of strain at the nanoscale.* Nature materials, 2009. **8**(4): p. 291-298.
45. Williamson, G. and W. Hall, *X-ray line broadening from filed aluminium and wolfram.* Acta Metallurgica, 1953. **1**(1): p. 22-31.
46. Dhara, S. and P. Giri, *Size dependent anisotropic strain and optical properties of strained Si nanocrystals.* J Nanosci Nanotechnol, 2011.
47. Viswanatha, R., et al., *Synthesis and characterization of Mn-doped ZnO nanocrystals.* The Journal of Physical Chemistry B, 2004. **108**(20): p. 6303-6310.
48. Chelikowsky, J.R., et al., *Computational studies of doped nanostructures.* Reports on Progress in Physics, 2011. **74**: p. 046501.
49. Schwartz, D.A., et al., *Magnetic quantum dots: synthesis, spectroscopy, and magnetism of Co2+-and Ni2+-doped ZnO nanocrystals.* Journal of the American Chemical Society, 2003. **125**(43): p. 13205-13218.
50. Radovanovic, P.V., et al., *Colloidal transition-metal-doped ZnO quantum dots.* Journal of the American Chemical Society, 2002. **124**(51): p. 15192-15193.
51. Dalpian, G.M. and J.R. Chelikowsky, *Self-purification in semiconductor nanocrystals.* Physical review letters, 2006. **96**(22): p. 226802.

52. Sung, Y.M., W.C. Kwak, and T.G. Kim, *Coarsening kinetics of Mn-doped CdSe nanocrystals.* Crystal Growth and Design, 2008. **8**(4): p. 1186-1190.

Appendix

```
#set prompt,redirect
#  nano.cdse.mac
#
########################################
##################
#
#  Main macro for the simulation of
#  cylindrical cdse nanowire
#
########################################
##################
#
variable integer,generation
variable integer,member
variable integer,children
variable integer,parameters
variable integer,kid
#
@setup
#
fclose all
fopen 1,GENERATION
fget  1,generation,member,children,parameters
fclose 1
#
do kid = 1,children
  fopen 2,"DIFFEV/Trials.%4D",kid
  fget  2,generation,member,children,parameters
  fget  2,i[1]
  @discus.cdse kid
  fclose 2
enddo
#
#exit
```

File:nano/setup.mac

```
#

#  allgemeiner setup
#
variable  integer,nindiv
#
nindiv = 1
```

File:nano/discus.cdse.mac

```
@variables.cdse
#
# Read the parameters from DIFFEV/Trials
fget 2
do i[3] = 1,parameters
  fget 2,r[200+i[3]]
enddo
#
read
stru CELL/cdse_wurtzite.cell
lat[1]   = r[201]
lat[2]   = r[201]
lat[3]   = r[202]
z[1]     = r[203]
b[1]     = r[204]
b[2]     = r[204]
p_stack  = r[205]
p_ab     = r[206]
p_cc     = r[207]

save
  outfile STRU/cdse_wurtzite.cell
  run
exit
@makelayers.cdse cdse_wurtzite
#
do indiv=1,nindiv
  @shape.cylinder cdse_wurtzite
  @ plot.xbs single_particle.bs
  @powder
  @output kid,indiv
enddo
```

File:nano/variables.cdse.mac

```
#
variable integer,indiv
#
variable real,  p_stack
variable real,  p_ab
variable real,  p_cc
#
```

File:nano/makelayers.cdse.mac

```
# makelayers.mac
#
variable integer,width
width = int(4.5* p_ab/r[201])
```

```
#
read
cell STRU/$1.cell,width,width,2
#
boundary hkl, 0, 0, 1,  0.5,inside
boundary hkl, 0, 0,-1,  1.3,inside
boundary cylinder,p_ab+2*lat[1],p_cc,inside
purge
#
save
  outf STRU/$1.layer
  write all
  run
exit
#
#@plot_xbs w1.xbs
#
symm
  angle 180.0
  type  proper
  mode  repl
  sel   all
  incl  all
  orig  0.333333, 0.666667, 0.00
  uvw   0,0,1
  trans 0.00, 0.00, 0.00
  run
exit
#
save
  outf STRU/$1.rotated
  run
exit
#@plot_xbs w2.xbs
```

File:nano/shape.cylinder.mac

```
#read
#cell STRU/$1.cell
@stack $1,p_stack
#@shift p_cc
#
@trans2cart
#@shear p_ab,p_cc
boundary cylinder,p_ab+2*lat[1],p_cc,inside
#
boundary hkl, 0, 0, 1, p_cc
boundary hkl, 0, 0, -1, p_cc
#@shear p_cc,p_ab
purge
#
save
  outf "STRU/$1.%4D.%4D.particle",kid,indiv
  omit  ncell
  omit  gene
  omit  scat
  omit  adp
  run
exit
#
@plot.xbs single_particle.bs
```

File:nano/stack.mac

```
#
# stapel.mac
#
variable integer,height
height = int(4.*p_cc/lat[3] + 2)
echo ####################################
eval p_cc
eval lat[3]
eval height
echo ####################################
#
stack
  layer STRU/$1.layer
  layer STRU/$1.rotated
  trans  1,1, -0.3333, 0.3333, 0.5000
  trans  1,2,  0.3333,-0.3333, 0.5000
  trans  2,1, -0.3333, 0.3333, 0.5000
  trans  2,2,  0.3333,-0.3333, 0.5000
  sigma  1,1,  0.0000, 0.0000, 0.0000
  sigma  1,2,  0.0000, 0.0000, 0.0000
  sigma  2,1,  0.0000, 0.0000, 0.0000
  sigma  2,2,  0.0000, 0.0000, 0.0000

  aver   0.00, 0.00, 1.00
  modu   1.00, 0.00, 0.00,  0.00, 1.00, 0.00
  set mod ,on
  set trans,fixed
#
  random prob,0.00
  random offset, 0.00, 0.00, 0.00
  random sigma , 0.00, 0.00, 0.00
#
  rotate status,off
#
  distr  matrix
#
  number height
#
  crow   1,      $2    ,1.00-$2
  crow   2,  1.00-$2    ,     $2
#
show
  create
  run
exit
```

File:nano/powder.cdse.mac

```
powder
  xray
  set axis,q
  set calc,debye
  set disp,off
  set delta,0.001123
  set qmin,1.000
  set qmax,12.000
  set dq,  0.0005
  set temp,use
  set wvle,0.496
  set four,four
```

```
  set lpcor,bragg,32.50
  run
exit
```

File:nano/trans2cart.mac

```
r[1] =  1.00/blen(2,1,0)
r[2] =  1.00/lat[2]
r[3] =  1.00/lat[3]
trans
  anew  2.*r[1], 1.0*r[1],  0.0
  bnew  0.0    ,     r[2],  0.0
  cnew  0.0    , 0.0     ,  r[3]
  onew   0.0, 0.0, 0.0
  sel all
  incl all
  run
exit
```

File:nano/output.mac

```
output
    form powder,tth
    value inte
    outf "POWDER/indi.%4D.%4D"  ,$1,$2
    run
  exit
```

File:nano/plot.xbs single_particle.bs´

```
plot
  prog cif
  uvw  0,0,1
  abs  1,0,0
  ord  0,1,0
  vect 0,0,0
  thick 1000
  outf "PLOT/$1.%4D.%4D.xyz",kid,indiv
  ext all
  sel all
  set cd,3, 1.0,1.0,1.0, 0.5
  set se,3, 1.0,0.0,0.0, 0.5

  run
exit
```

Acknowledgement

It is a pleasure to thank those people whose contribution made this thesis possible. I would like to convey my gratitude to all of them with my humble acknowledgement.

First and foremost, my utmost gratitude to Prof. Dr. Ullrich Pietsch for giving me the opportunity to write this thesis and guidance from preliminary to concluding level. I am deeply grateful for your advice, support, encouragement, regular enjoyable meetings and useful discussions about the progress of my research throughout the working period.

I gratefully thank Dr. Zhen Li for providing me all samples and TEM images.

I would like to extend my deep thanks to Dr. Ozgul Kurtulus, Andreas Biermanns, Anton Davydok, T.S. Sabi for help me during the samples measurement in synchrotron and valuable advice in scientific discussion.

Many thanks go in particular to Prof. Dr. Reinhard Neder, for helping to run the DISCUS software and providing the macro files for the simulation.

I would like to express my gratitude to Dr. Tusar Sant for guiding me at early stage of my thesis period.

I would also like to thank BL9 (Delta Dortmund) and P08 (PETRA III Hamburg) beamline scientists for providing the beamline and experimental support.

I would like to thank all group members of FKP group of University of Siegen who contributed directly or indirectly in performing this master thesis especially for Saqib, Tahir and Kamran having good time and encouragement during the thesis period.

Last but not the least, I would like to thank my family for deep love, and financial support.

Erklärung

Hiermit erkläre ich, dass ich die vorliegende Masterarbeit selbständig verfasst und keine anderen als die angegebenen Quellen und Hilfsmittel benutzt, sowie Zitate und Ergebnisse Anderer kenntlich gemacht habe.

…… ……..

(Ort) (Datum) (Unterschrift)